Friction https://mc03.manuscriptcentral.com/friction
https://doi.org/10.26599/FRICT.2026.9441265

Research Article

Fabrication of hierarchical pillar-structured superhydrophobic surfaces on titanium alloy for underwater drag reduction via a hybrid micro/nano-texturing method

Bin Zhao[1], Jianfu Zhang[2], Peiyuan Ding[2], Pingfa Feng[2], Qilin Li[2], Hang Yu[2], Ding Weng[2], Daochun Xu[1*], Jianjian Wang [2*]

[1] *School of Technology, Beijing Forestry University, Beijing, 100083, China*

[2] *State Key Laboratory of Tribology in Advanced Equipment, Department of Mechanical Engineering, Tsinghua University, Beijing, 100084, China*

* Corresponding author: Jianjian Wang, wangjjthu@tsinghua.edu.cn

Received: December 4, 2025; Revised: April 4, 2026; Accepted: May 7, 2026

Abstract: Constructing superhydrophobic micro/nano-hierarchical surfaces is an efficient means of reducing hydrodynamic drag on underwater vehicles. Titanium alloys, owing to their high strength and corrosion drag, have become essential structural materials for such applications. However, most existing surface-structuring approaches for titanium alloys rely on a single fabrication technique. This limitation constrains further improvements in drag-reduction performance. To address this challenge, this study proposes a multi-process composite fabrication approach that integrates the advantages of three complementary techniques to produce micro/nano-structured superhydrophobic titanium alloy surfaces. Phase-controlled vibration micro-texturing (PVMT) is first applied to generate microscale pillar structures; ultrafast laser nano-texturing (ULNT) is then used to machining nanoscale structures; finally, surface energy modification (EM) is conducted through fluorination treatment. The PVMT technique is newly proposed in this work. By precisely controlling the phase difference between two cutting passes, the material removal behavior is regulated such that the residual material forms discrete micropillar arrays, which is favorable for enhancing drag-reduction performance. To verify the performance of this hybrid approach, titanium alloy samples were prepared under various process parameters, followed by wettability characterization and underwater drag measurements using a custom-built testing platform. Wettability results show that PVMT significantly improves hydrophobicity, increasing the static contact angle from 78.6° to 112.4°. When combining PVMT&ULNT&EM, the contact angle rises to 154.2°, demonstrating superhydrophobic behavior. Drag tests reveal that PVMT generated micropillar structures can reduce drag by up to 12.6%. With additional ULNT and EM treatments, the drag-reduction rate increases to a maximum of 22.1%, among the highest drag-reduction values reported for titanium alloy surfaces. Additionally, the surface drag reduction performance is recoverable. These experimental results confirm the efficiency of PVMT in constructing functional micropillar arrays, and validate the effectiveness of the PVMT&ULNT&EM composite process in fabricating hierarchical superhydrophobic surfaces for enhanced underwater drag reduction. This approach offers a promising route for functionalizing advanced underwater engineering materials.

Keywords: Underwater drag reduction； Hierarchical pillar structures； Superhydrophobic surfaces； Vibration cutting； Laser machining.

1 Introduction

With the increasing demand for energy-saving technologies in various industrial and marine engineering applications, reducing hydrodynamic drag has therefore become an important research focus [1–2]. In practical application such as pipeline transportation, underwater vehicles, and ships, surface friction drag accounts for about 50% of the total drag [3]. Reducing surface friction drag during underwater movement can significantly improve energy efficiency and overall performance during underwater navigation and transportation [4]. For underwater unmanned vehicles, reduced drag also enhances underwater endurance capability. To meet requirements for endurance, corrosion drag, high pressure drag, and stealth, titanium alloy has become an ideal structural material for underwater unmanned vehicles due to its low density, high strength, corrosion drag, and non-magnetic characteristics [5]. Thus, constructing drag reducing functional surfaces on titanium alloys is of significant importance and need.

Currently, underwater drag-reduction strategies can be divided into active drag reduction and passive drag reduction. Active drag reduction relies on continuous injection of polymers [6] or air bubbles [7-8], but these methods are costly and may cause environmental pollution. Passive drag reduction does not require external energy input or material consumption. It achieves drag reduction through spontaneous interactions during navigation. Its low cost and environmental friendliness have attracted wide attention. Passive drag-reduction concepts come from microstructure biomimicry. Representative examples include the super-hydrophobicity and self-cleaning ability of lotus leaves [9], the drag reducing properties of shark skin [10], and butterfly wings [11-12]. These functions arise from the interaction between micro/nano scale surface structures and surrounding fluids. Inspired by these surfaces, by fabricating micro-nano structures on the material surface [13] or spraying coatings to reduce surface energy [14-15], or combining both methods, the hydrodynamic behavior in the near-wall region can be altered to achieve drag reduction.

Efficient and controllable fabrication of micro/nano drag-reduction structures is essential for engineering applications. The mainstream methods of the micro-nano structures include the template method [16], ultrafast laser ablation [17], vapor deposition [18], electrical discharge machining [19], anodizing [20], boiling-water oxidation [21], mechanical machining [22] and Compound processing method [23]. The template method excels in large area fabrication efficiency but is unsuitable for hard materials such as titanium alloys. Ultrafast laser etching has the advantages of high precision and wide range of applicable materials, and is good at rapid processing of nano-scale structures, but it has the problem of low efficiency in microstructure processing. The uniform films prepared by vapor deposition method have the characteristics of high consistency and strong adhesion, but the processing freedom is limited, and it is difficult to construct typical drag reducing structures such as grooves and bumps. Electrical discharge machining can process titanium alloys, but it is difficult to process the small-scale microstructure. Chemical methods such as anodizing and boiling water oxidation can realize the large area and high efficiency nanoscale structures, but the processing ability of microscale structures is limited. The compound processing method integrates multiple fabrication techniques to collaboratively construct drag reducing micro/nano structures.

Vibration cutting, a representative micro-nano structure machining method, is well suited for metals like titanium alloys. It offers distinct advantages including precise surface morphology control, high processing efficiency, preservation of the material's chemical composition, and effective regulation of subsurface damage behavior [22-24]. It also has high process flexibility. By flexibly selecting processing methods and precisely controlling process parameters such as cutting speed, vibration frequency, amplitude, and tool path, various microscale morphologies can be fabricated on material surfaces, including pillars [25], pits [26], grooves [27-29], and riblets [30]. Verified applications include surface structural coloration [31-32], thermal conduction regulation [33], surface friction control [34], biological applications [35], and surface wettability engineering [36-37]. In the field of surface wettability regulation, studies have demonstrated that vibration cutting microstructures can effectively improve material hydrophobic properties. According to wetting theory [38], surface hydrophobicity strongly influences underwater drag. Increased hydrophobicity reduces adhesion and interfacial friction, lowering frictional drag. Thus, vibration cutting microstructures have both theoretical and engineering value for underwater drag reduction.

However, current vibration cutting for microstructure preparation has not yet been applied directly to underwater drag reduction surfaces. For Ti-6Al-4V, the current processing technology utilizes the pit-digging principle to efficiently fabricate concave microstructures with a low aspect ratio. In theory, high aspect ratio pillars could be fabricated using tapered tapered-tip single-crystal diamond tool, enabling stable gas retention interfaces and improved hydrophobicity and drag reduction. However, relying solely on vibration cutting is insufficient to maximize the aforementioned performance. Laser processing techniques have also been widely employed for the fabrication of functional micro–nano surfaces. By tailoring the processing parameters, multiscale structures can be generated on metallic composite surfaces, enabling the achievement of superhydrophobic properties [39]. Nevertheless, high-energy laser processing alone may alter the physical characteristics of the material's surface layer. In summary, existing fabrication methods can produce hydrophobic micro/nano structures, but each has limitations in efficiency, precision, material compatibility, and morphology control. Achieving flexible micro/nano structuring on titanium alloys remains challenging and restricts optimal drag reduction performance.

To overcome these limitations, this study proposes a multi-scale composite fabrication strategy. A new vibration cutting process is first developed to construct microscale structures on Ti-6Al-4V. Femtosecond laser scanning is then applied to form nanoscale textures. A thin chemical coating is finally used to adjust surface energy and enhance hydrophobicity. **Fig. 1** illustrates a schematic representation of a superhydrophobic surface with hierarchical pillar structures applied to an underwater vehicle, demonstrating its function in reducing hydrodynamic drag during navigation. This paper first presents the PVMT machining principle, and then carries out the microstructure processing experiment on Ti-6Al-4V to verify its effectiveness in the manufacturing process of high efficiency micropillars. On this basis, the combined PVMT&ULNT&EM process is further evaluated for improving hydrophobicity and reducing underwater frictional drag.

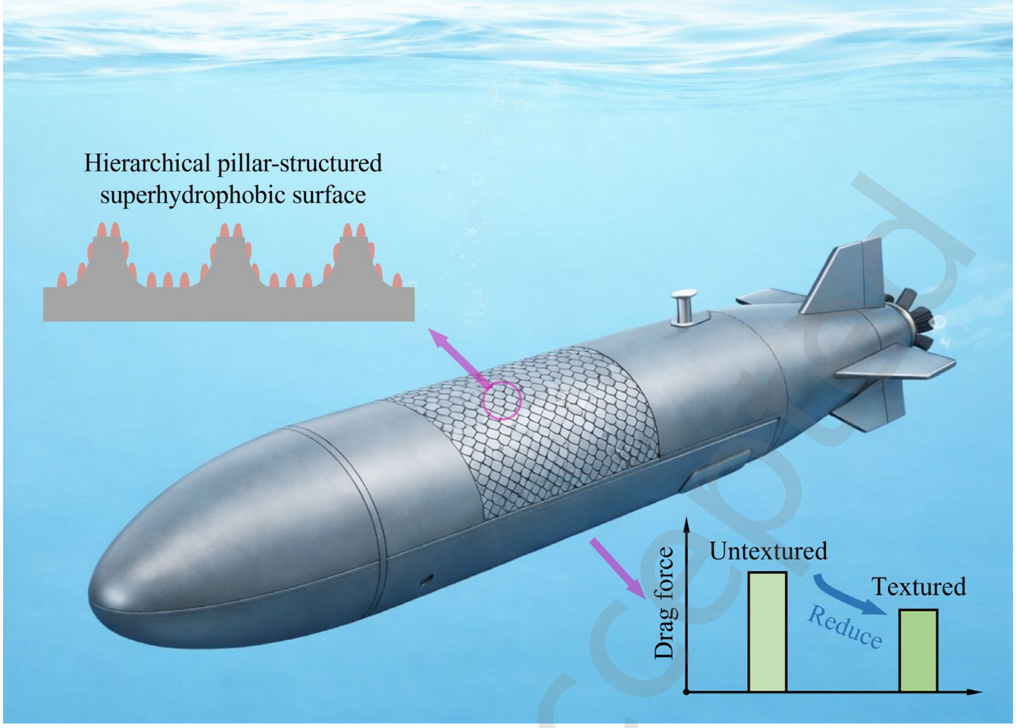

Fig. 1 Schematic diagram of micro/nano structure drag reduction on underwater vehicle.

2 Principle of combined method

2.1 Hybrid method

The present study proposes a multi-process composite surface fabrication strategy for titanium alloys. As shown in **Fig. 2**, the integration of three processing techniques—phase-controlled vibration micro-texturing (PVMT), ultrafast laser nano-texturing (ULNT), and surface energy modification (EM) are integrated to combine the advantages of each individual technique for constructing composite micro/nano interfaces with hierarchical structures and low surface energy. First, as shown in **Fig. 2**a, the PVMT technique is employed to fabricate regular and controllable micro-pillars arrays on the Ti-6Al-4V substrate by removing material through cutting, thereby providing the foundation for subsequent multi-scale texturing. Next, as shown in **Fig. 2**b, the ULNT technique is applied to further inscribe nanoscale surface textures on the micropillar structures, introducing finer roughness and hierarchical morphology. Finally, as shown in **Fig. 2**c, the EM technique is used to modify the previously formed hierarchical micro/nano structures to achieve low surface energy, thereby further enhancing the hydrophobic properties of the surface. This study provides a new technological pathway for underwater drag reduction and functional surface fabrication.

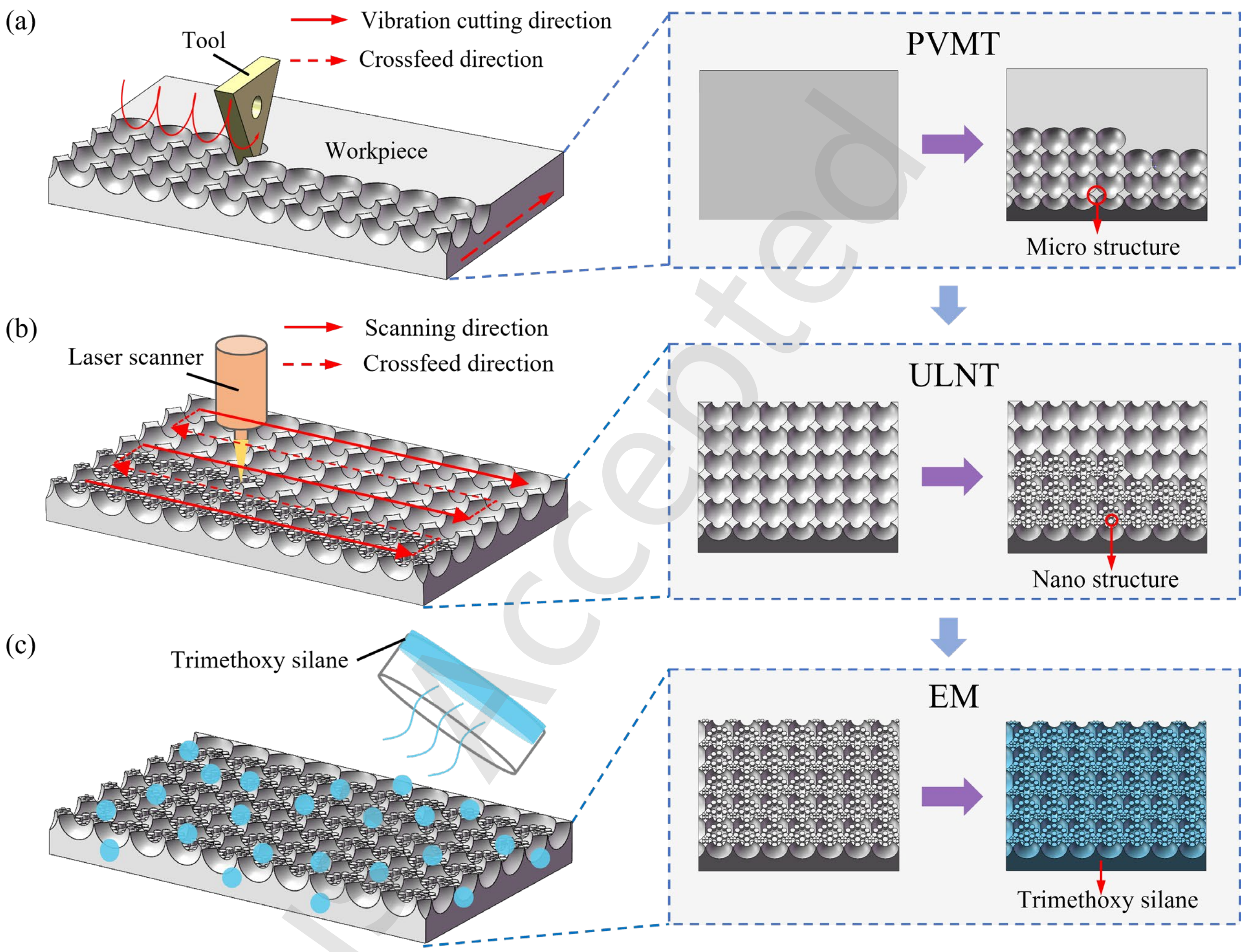

Fig. 2 Schematic diagram for fabrication of hierarchical Micropillars superhydrophobic surfaces. (a) Schematic diagram of the proposed phase-controlled vibration micro-texturing (PVMT). (b) Schematic diagram of ultrafast laser nano-texturing (ULNT). (c) Schematic diagram of surface energy modification (EM).

2.2 Phase-controlled vibration micro-texturing

The fabrication of micropillar structures is a key step in this study. To achieve this, a phase-controlled vibration micro-texturing (PVMT) method is proposed. **Fig. 3**a illustrates the PVMT processing principle, in which the X, Y, and Z axes correspond to the cutting direction, cutting depth direction, and transverse feed direction, respectively. During machining, the vibration device imposes an elliptical trajectory on the tool in the XOY plane, while the tool simultaneously performs unidirectional linear motion along the cutting direction. As a result, the cutting depth dynamically varies with the tool displacement throughout the machining process, enabling precise control of microstructure formation. A forward-elliptical trajectory is selected in this study, and the ellipse is set to rotate clockwise to compensate for the morphological deviations of machined pits caused by the difference between the tool's rake angle and clearance angle. The semi-major axis a of the ellipse is aligned with the y-axis, and the semi-minor axis b is aligned with the x-axis. As shown in **Fig. 3**b, within each vibration cycle, the tool periodically enters and exits the workpiece surface along the elliptical trajectory, removing material and generating micro-pits when the tool penetrates into the workpiece. Based on pit formation, independently controlled micropillars can be produced by regulating the phase difference between two cutting passes, so that the remaining material becomes discrete pillars with controllable height. Using this principle, a periodic and dimensionally consistent micropillar array is progressively formed on the material surface with continuous multi-pass machining.

The machining parameters of the microstructure fabrication process mainly include the elliptical vibration trajectory parameters, vibration frequency f, tool geometry (for a carbide-tipped tool, the tool tip arc radius R), cutting depth (DOC), nominal cutting velocity v_c, cross feed between adjacent passes f_z, and phase difference P (0° and 180°) between adjacent passes. Among these parameters, the tool motion trajectory is the most essential factor for realizing microstructure machining. The trajectory can be decomposed into two components along the cutting direction (X-axis) and the cutting-depth direction (Y-axis). Under constant cutting speed and initial cutting depth, the actual tool trajectory during machining can be precisely regulated through elliptical vibration. The actual motion trajectory of the tool can be expressed by the following parametric equations:

$$\begin{cases} x(t) = b\cos(2\pi ft) + vt \\ y(t) = a\left[\sin(-2\pi ft) - 1\right] + DOC \end{cases} \tag{1}$$

where $x(t)$ and $y(t)$ represent the time-dependent displacements of the tool along the x-directions and y-directions, respectively. The parameters a and b denote the semi-major and semi-minor axes of the elliptical trajectory. By adjusting the input voltage applied to the piezoelectric actuators of the vibration device, the above elliptical trajectory parameters can be tuned, enabling arbitrary elliptical trajectories of the tool within the XOY plane.

In PMVT, the distribution of micro-pits can be precisely controlled to achieve optimal material removal connectivity only when process parameters meet specific matching relationships. Meanwhile, the uncut material forms isolated micropillars structures. In this process, the generation of micro-pits serves as the foundation. The relationship between the micro-pit geometry and the process parameters is expressed as follows:

$$\begin{cases} t_x = \dfrac{\pi - 2\arcsin\left(1 - \dfrac{DOC}{a}\right)}{2\pi f} \\ r_z = 2\sqrt{R^2 - \left(R - DOC\right)^2} \\ r_x = vt_x \\ l_x = \dfrac{v}{f} \end{cases} \tag{2}$$

where r_z represents the length of the pit in the transverse feed direction within per vibration cycle, r_x represents the pit length in the cutting direction within per cycle, l_x denotes the tool movement distance along the x-axis within per cycle, and t_x is the effective cutting time during a per cycle.

$$\begin{cases} L = \sqrt{l_x^2 + f_z^2}, & \text{if } P = 0° \\ L = \sqrt{\left(\dfrac{l_x}{2}\right)^2 + f_z^2}, & \text{if } P = 180° \end{cases} \tag{3}$$

where L denotes the distance between the center points of two staggered pits in adjacent machining rows.

$$\begin{cases} \varphi = \arctan\left(\dfrac{f_z}{L}\right) \\ r = \dfrac{DOC}{a}\sqrt{r_x^2\cos^2\varphi + r_z^2\sin^2\varphi} \end{cases} \tag{4}$$

where the φ indicates the angle between the line connecting these two center points and the horizontal direction, and r denotes the distance from the center point of the pit to the pit edge along the line connecting the two points.

The matched control of the pit geometry and distribution is crucial for achieving the fabrication of micro-pillar structures. The corresponding conditions are discussed as follows:

1) When $r_z < f_z$ or $r_x < l_x$, as shown in **Fig. 3**f, only pit-shaped micro structures similar to those produced by conventional vibration cutting are generated, and the desired pillar structures cannot be formed. As illustrated in **Fig. 3**c, traditional pit machining only produces isolated concave units on the surface, failing to utilize the residual material left by cutting to construct continuous geometric features.

2) When $r_z > f_z$, the material between adjacent tool paths becomes separated in the x-direction, resulting in partial overlap of pits along this direction. Moreover, when $DOC \geq 2a$, with $t_x = 1/f$ and $r_x = l_x$, meaning that the remaining material in the z-direction also becomes separated and the pits along this direction partially overlap. When the cutting residues in both directions are simultaneously separated, micro-pillar structures are formed on the material surface. As shown in **Fig. 3**d and **Fig. 3**e, these are schematic diagrams of micro-convex structures with longitudinal phase parallel and longitudinal phase staggered configurations processed by this method, respectively. The structure morphology is obviously different with the regulation of the phase relationship. If only one direction satisfies the condition, the pits will simply overlap in that direction, and no isolated pillars can be produced.

3) When $r > \dfrac{L}{2}$, as shown in **Fig. 3**g, the pits fully cover the machined surface, leading to extensive overlap between pits and leaving no uncut material region. Although residual pillars remain dispersed

on the surface, their large spacing and limited size prevent the formation of a continuous microstructure, rendering them functionally insignificant for the interface properties.

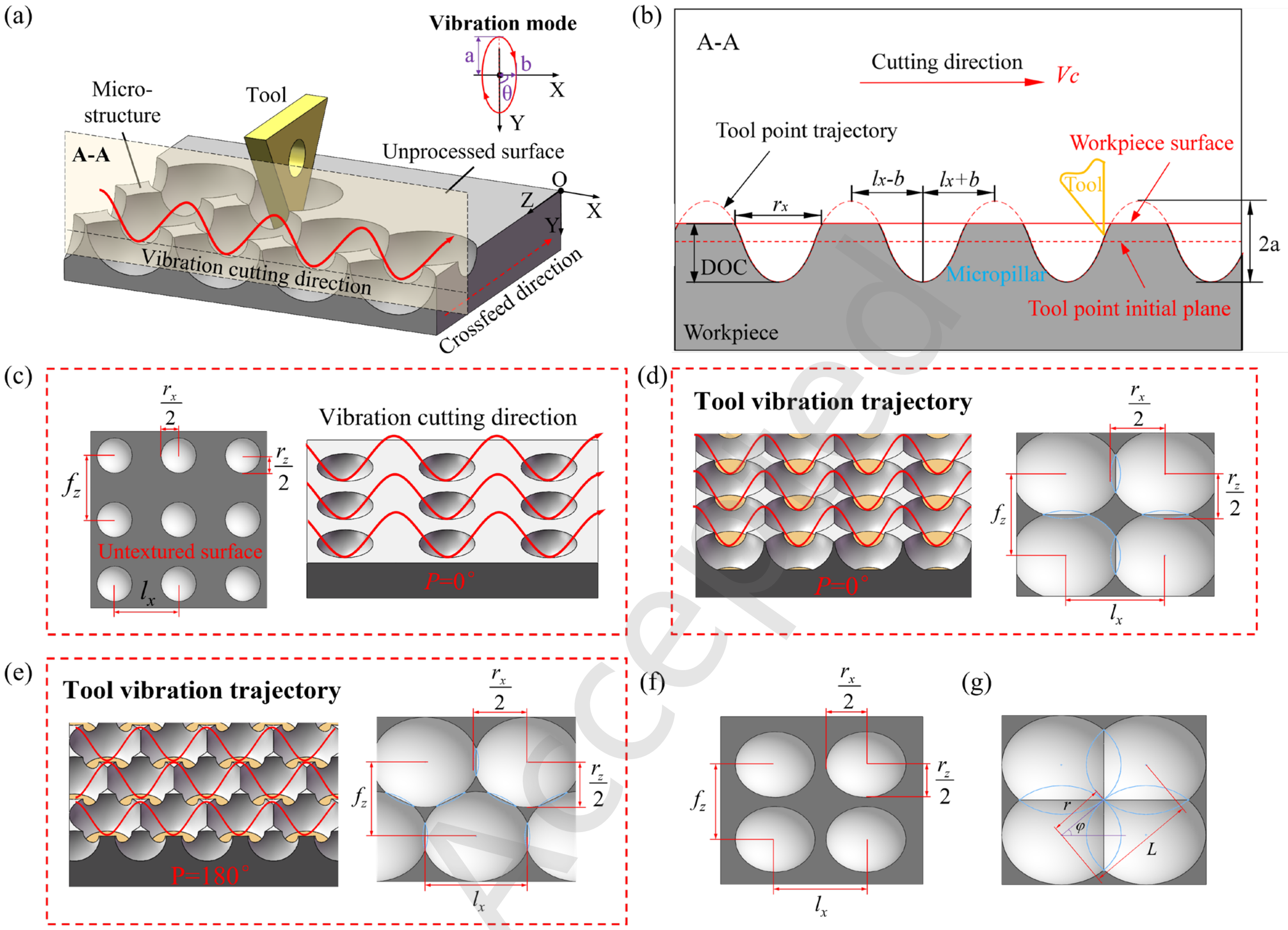

Fig. 3 (a) Schematic diagram of the proposed PVMT. (b) Schematic machining diagram of material removed by cutting and relevant machining parameters. (c) Schematic diagram of conventional dimple machining. (d) Schematic diagram of longitudinally parallel PVMT. (e) Schematic diagram of longitudinally interlaced PVMT. (f) Schematic diagram of machining without overlapping of dimple. (g) Schematic Diagram of Excessive Overlap Machining of dimple.

3 Experimental design

3.1 Vibration texturing

To evaluate the effectiveness of PVMT and to determine suitable processing parameters, machining experiments were conducted using Ti-6Al-4V titanium alloy plates (75 mm×25 mm×2 mm, China) were selected as substrates. The vibration cutting machining platform adopts the four-axis ultraprecision machining platform, as shown in **Fig. 4**a. The platform consists of a three-axis nanopositioning stage (X/Y/Z axes) and a linear actuator (XX axis, Aerotech, U.S.A.), the mechanically polished workpieces were fixtured onto the nanopositioning stage. The stage holds the workpiece stationary in the XOY plane and provides transverse feed motion along the Z axis, while the linear actuator controls tool motion along the XX axis. Before cutting, the workpiece surface was leveled to ensure parallelism between the sample surface and the XOZ plane.

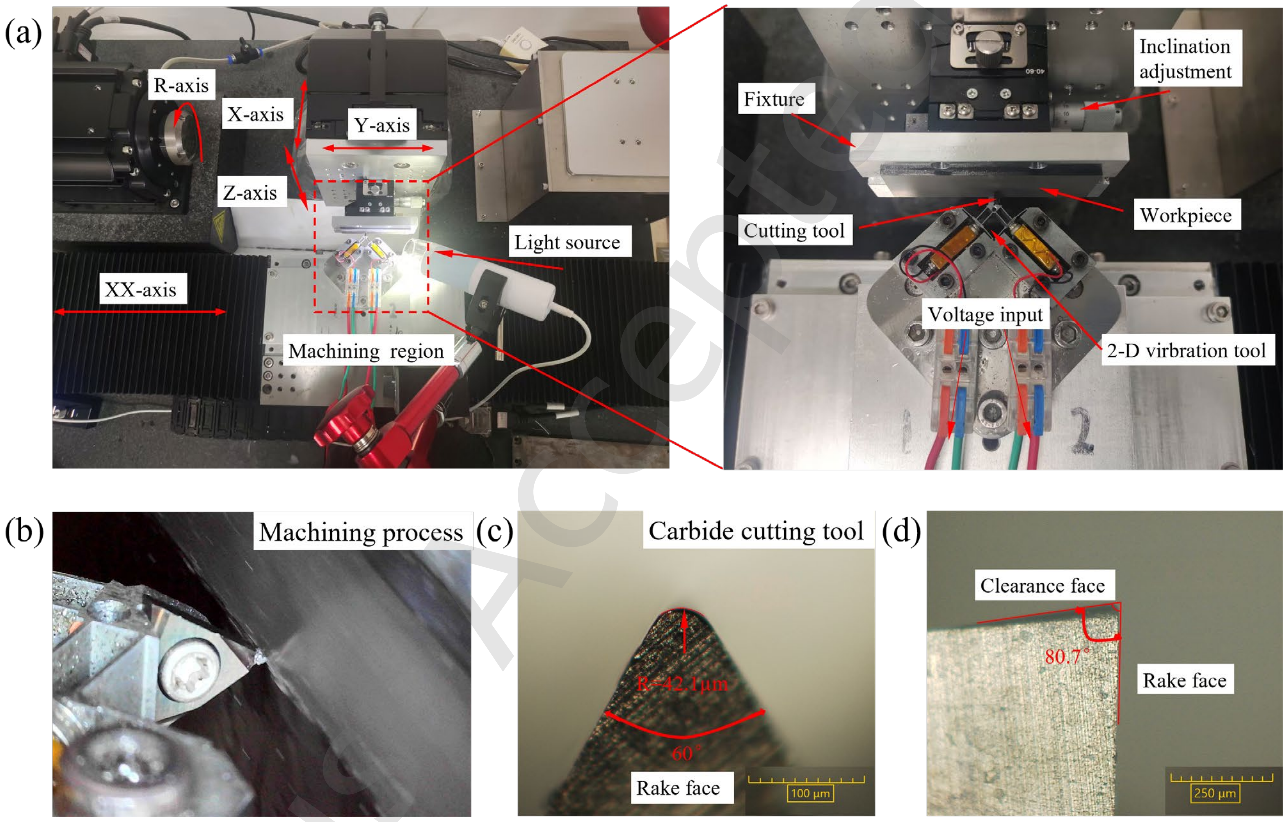

Fig. 4 (a) PVMT experimental device. (b) Photograph of PVMT processing. (c)&(d) Photograph of cutting tool.

The machining experiments employed a carbide-tipped tool with an angle of 60°, a rake angle of 0°, a clearance angle of 9.3°, and a tool-tip radius of 42.1 μm, as shown in **Fig. 4**c and **Fig. 4**d. The tool was fixed on the vibration cutting device as shown in **Fig. 4**b. The elliptical vibration was generated by voltage signals from the signal generator (Aim-TTi, TG5012A), amplified using the power amplifier (PiezoDrive, PX200), and transmitted to two piezoelectric stacks (PK4FQP1, Thorlabs). The two piezoelectric stacks generate two sine displacement trajectories in the XOY plane, which are perpendicular to each other, and their coupled motion generated the required elliptical trajectory.

To investigate the effects of different processing parameters on microstructure characteristics, systematic experiments were conducted by varying the cutting speed, vibration frequency, initial cutting depth, and elliptical vibration parameters. The research aimed to explore how these parameters, particularly micro-pillars surface morphology and phase difference, influenced experimental results. To study the influences of cutting depth, microstructure phase distribution, and aspect ratio on subsequent hydrophobicity and underwater drag tests, nine groups of cutting conditions were designed, as listed in **Table 1**. After machining, all samples were ultrasonically cleaned in anhydrous ethanol, acetone, and deionized water for 10 minutes each, and then dried for subsequent testing.

Table 1 Parameters of elliptical vibration cutting process

No.	$S=v_c/f$ (μm)	Vibration frequency f (Hz)	*DOC* (μm)	Cross feed f_z (μm)	Trajectory (μm)	Adjacent row phase *P*
PVMT1	50	500	6	35	$a=3$，$b=1$	180°
PVMT 2	50	500	8	40	$a=4$，$b=1$	180°
PVMT 3	50	500	10	45	$a=5$，$b=1$	180°
PVMT 4	50	500	6	35	$a=3$，$b=1$	0°
PVMT 5	50	500	8	40	$a=4$，$b=1$	0°
PVMT 6	50	500	10	45	$a=5$，$b=1$	0°
PVMT 7	40	600	6	35	$a=3$，$b=1$	180°
PVMT 8	40	600	8	40	$a=4$，$b=1$	180°
PVMT 9	40	600	10	45	$a=5$，$b=1$	180°

3.2 Ultrafast laser nano-texturing and surface energy modification

Femtosecond laser was performed on the PVMT-processed samples and the untextured samples to introduce nanoscale structures onto the pre-machined microscale structures, thereby forming hierarchical micro/nano composite surfaces. The femtosecond laser processing was conducted using a galvanometer scanning system. The ULNT process was independent of the PVMT process, and no re-alignment between the two procedures was required. The processing procedure is shown in **Fig. 5**a. The scanning was carried out with a circularly polarized femtosecond laser with a central wavelength of 1030 nm and a repetition frequency of 300 kHz. The scanning power was 29.4 W, corresponding to a single pulse energy of 58.8 μJ. The scanning direction was along the above figure and the scanning speed was 100mm/s. The spacing between adjacent two scanning rows was 14μm. Prior to processing, the initial focal position of the laser was precisely aligned using a CCD camera. Under the above processing parameters, the surface was scanned three times to generate irregular nanoscale rough structures. The ULNT scanning area was significantly larger than the micro-protrusion region fabricated by PVMT. All laser processing was conducted at room temperature. **Fig. 5**c shows the ULNT processing setup. After laser ablation, the samples were ultrasonically cleaned in anhydrous ethanol, acetone, and deionized water for 5 min each, followed by drying for subsequent experiments.

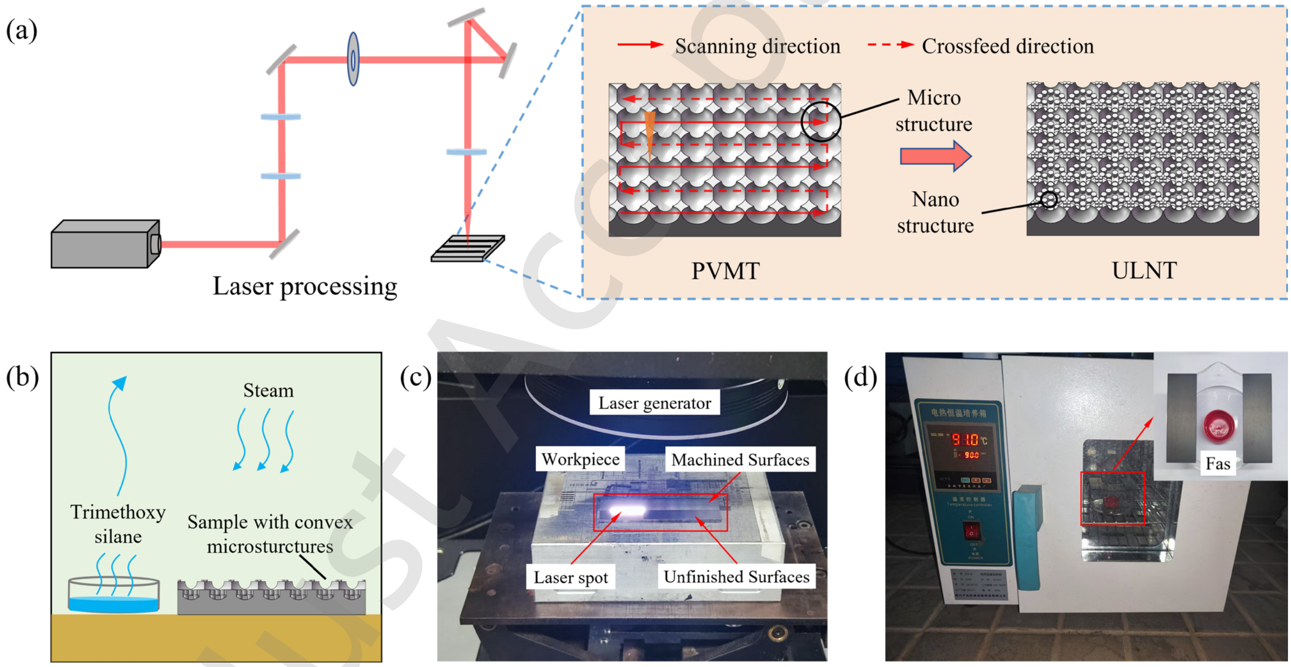

Fig. 5 (a) Schematic diagram of ULNT. (b) Schematic diagram of EM. (c) Photograph of ULNT processing. (d) Photograph of EM treatment device.

For the control samples, fluorination treatment was applied to: (i) PVMT samples, (ii) ULNT samples, and (iii) samples sequentially treated with PVMT and ULNT. The fluorination procedure is shown in **Fig. 5**b. Trimethoxy (1H,1H,2H,2H-heptadecafluorodecyl) silane (F.A.S.) (Macklin, China) was selected as the reagent for EM surface modification. A total of 0.5 g of F.A.S. was placed in a petri dish, and the samples were heated in a constant-temperature drying oven at 90 °C for 4 h [19].

During this process, the reagent vaporized and uniformly deposited onto the sample surfaces, forming a stable hydrophobic coating. **Fig. 5**d illustrates the EM processing setup.

3.3 Basic physical and chemical property test of surface

For the processed sample surfaces, a contact angle measuring instrument (CAST SL250, Kino, U.S.A.) was used to measure the static water contact angles. The surface morphology, microstructure and elemental distributions of the samples were obtained by using the Super Depth Microscope (HRX-01, Hirox, China), white light interferometer (Zygo, Nexview, USA) and scanning electron microscope (ZEISS, sigma 500, Germany).

3.4 Underwater resistance test platform

3.4.1 Resistance test device

To quantitatively evaluate the drag reduction performance of the fabricated micro/nano composite titanium alloy surfaces under dynamic water flow conditions. As shown in **Fig. 6**, this study independently designed and constructed an underwater flow drag testing system. **Fig. 6**a shows the overall schematic of the drag testing device, **Fig. 6**b illustrates the structure of the test section, and **Fig. 6**c provides an enlarged view of the local test section. The system consists of a circulating water circuit, a sample mounting module, and a mechanical measurement unit. The sample is fixed onto a transparent acrylic cover plate and connected to a high-sensitivity pressure sensor through a force transmission shaft. The circulating water is driven by the pump into the test channel, and the flow rate is regulated by the precision control valve. Meanwhile, the flowmeter monitors the flow rate in real time to ensure the repeatability and stability of the test conditions.

During test process, water flows uniformly across the sample surface along the direction shown in **Fig. 6**a. The interaction between the water flow and the surface generates a tangential hydrodynamic drag force in the flow direction. This drag is transmitted through the force transmission shaft to the pressure sensor and converted into corresponding pressure signal. The pressure sensor records the instantaneous pressure data at high sampling frequency for each preset flow velocity, and the average value of the steady-state region is taken as the drag force at that condition. To reduce the external interference, the device was strictly zero-point calibrated and static pressure compensated before the test. and the water temperature was kept stable during the test constant to avoid the additional variables caused by the hydrodynamic viscosity. To ensure measurement reliability, each flow rate was measured three times and averaged statistically to reduce random disturbance induced deviations.

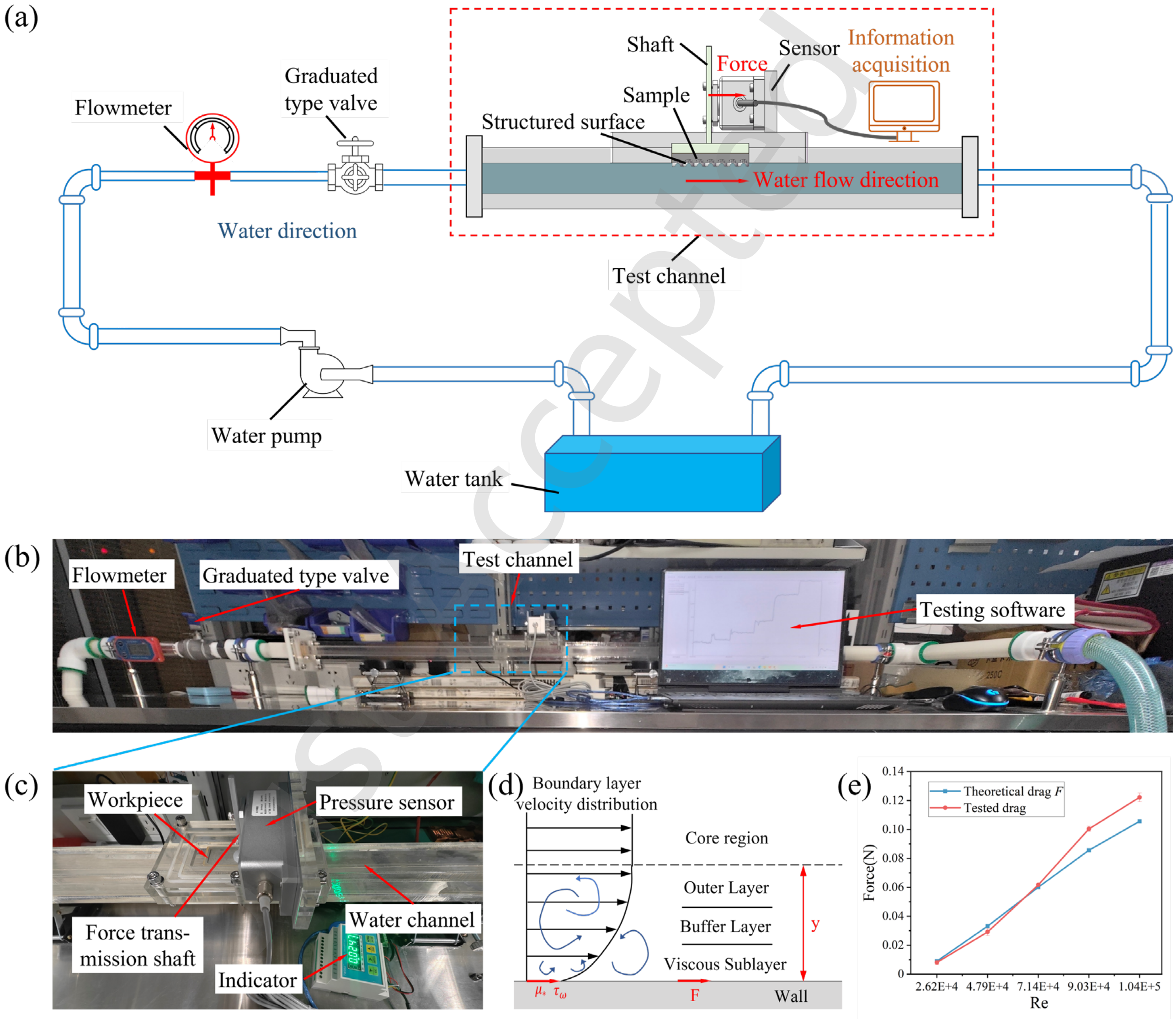

Fig. 6 (a) Schematic diagram of drag test device. (b) Drag test device. (c) Drag test section device. (d) Distribution of turbulent boundary layer on material surface. (e) Theoretical drag *F* and device test drag.

3.4.2 Calculation of water drag

Before conducting drag reduction experiments, the reliability of the measurement system was validated using a smooth reference sample by comparing the experimental data with theoretical predictions. The flow medium used in this experiment is tap water at 25 °C, and the distance between the sample center and the pipe inlet was fixed at l = 0.5 m. The validation procedure involved three steps:

1) First, determination of flow state near the sample surface. Taking the smooth control sample as an example, **Fig. 6**d shows the turbulent boundary layer distribution on the material surface. Assuming a maximum flow velocity of V_{max} = 4 m/s and the Reynolds number for the plate boundary layer transition is $\mathrm{Re}_x = 6\times10^5$, the flow transitions from laminar to turbulent [40].

The friction coefficient C_{f1} under turbulent conditions [41] can be expressed as,

$$C_{f1} = \frac{0.074}{\sqrt[5]{\mathrm{Re}}} \tag{5}$$

The corresponding wall shear stress τ_ω [41] is,

$$\tau_\omega = \frac{1}{2} C_{f1} \rho V_{\max}^2 \tag{6}$$

Due to the non-uniform velocity distribution in the test channel, near-wall flow exhibits interfacial slip. The friction velocity μ_* of the fluid near-wall is,

$$\mu_* = \sqrt{\frac{\tau_\omega}{\rho}} \tag{7}$$

The vertical distance $y^+\approx5$ marks the boundary between the laminar flow layer and the turbulent layer. The boundary y between turbulent and laminar flow at the base layer is calculated as follows [41],

$$y = \frac{y^+ \vartheta}{\mu_*} \tag{8}$$

Among them, ϑ is the kinematic viscosity of tap water at 25°C, calculated as y=0.042mm. Since the height of the microstructures is much smaller than the thickness of the boundary layer, their influence is primarily confined to the viscous sublayer. The drag reduction is achieved by modifying the near-wall velocity gradient and redistributing the shear stress, without disrupting the overall development of the boundary layer. Consequently, the near-wall flow remains in a laminar state. When the flow velocity is lower than V_{max} , the corresponding y further increases, yet the flow continues to maintain laminar characteristics. Therefore, throughout the entire range of tested flow velocities, the flow regime remains laminar.

2) Then, Calculation of theoretical drag on the smooth surface. The sample is a Ti-6Al-4V plate of dimensions 75mm×25mm×2mm. The Reynolds number Re of the boundary layer [42] is,

$$\mathrm{Re} = \frac{\mu_* l}{\vartheta} \tag{9}$$

The friction coefficient C_f for laminar boundary layer flow on a smooth flat plate [41] is,

$$C_f = \frac{1.328}{\sqrt{\mathrm{Re}}} \tag{10}$$

The theoretical underwater frictional drag F_* on the sample surface is [41],

$$F_* = \frac{1}{2} c_f \rho v^2 A \tag{11}$$

where v is the flow velocity in the test section, and A =75 mm×25 mm is the stress area of the sample.

Since components like the waterproof sealing ring and cover plate inside the device generate additional frictional resistance during actual testing, a correction factor ε is applied to correct the drag test results [43], yielding the corrected test drag,

$$F = \varepsilon F_* \tag{12}$$

The calculated value F corresponds to the drag measured by the system.

3) For the smooth sample, **Fig. 6**e compares the theoretical drag and measured drag of the sample surface. The deviation is within 15%, confirming the accuracy and reliability of the measurement system.

4 Results and discussion

4.1 Results after PVMT

4.1.1 Vibration texturing results and surface morphology characterization

By employing the PVMT processing method, micro-pillar structures with controllable dimensions and morphologies were successfully fabricated. **Fig. 7** presents the experimental results of the microstructured surface morphology obtained under various processing parameters. Due to the relatively high cutting speed, the short semi-axis b of the control ellipse vibration lateral displacement has little effect on the machining trajectory, and the machining trajectory is close to the standard sine trajectory, so b=1 is set. As shown in the "expected processing" images, group PVMT1-PVMT3 achieved microstructure morphology control by adjusting cutting depth (*DOC*), cross feed (f_z), and the major axis (a) of the elliptical vibration trajectory, while maintaining constant cutting speed (v_c), vibration frequency, and consistent longitudinal staggered phase (P = 180°). The results indicate that increasing the depth of cut leads to a higher aspect ratio of the micro-pillar structures. Group PVMT4–PVMT6 correspond to PVMT1–PVMT3, respectively, under the condition that other processing parameters were unchanged, the phase difference P was adjusted from 180° to 0°, so that the morphology of the microstructure changed from longitudinally staggered to longitudinally parallel. Similarly, group PVMT7–PVMT9 correspond to PVMT1–PVMT3, in this case, under the condition of keeping other processing parameters constant, the transverse length of the micro-pillar is changed by adjusting the v_c and f, thus improving the depth-to-width ratio of the microstructure. The theoretical dimensions of the micro-pillar structure on the surface participating material are shown in the figure.

As shown in the **Fig. 7**, the microscopic morphological characteristics of the microstructured surfaces are clearly presented. The scanning electron microscope (SEM) images reveal the pit-like structures formed through material removal, as well as the protruding regions on the processed surface. The machined pits exhibit an approximately elliptical shape with curved edges. Fine, scale-like textures appear inside the pits, resulting in relatively rough internal surfaces. This phenomenon primarily stems from the low hardness and low thermal conductivity of Ti-6Al-4V. During cutting, the generated heat cannot be efficiently dissipated through the chips or the workpiece, causing a sharp temperature rise on the shear plane. Consequently, thermal softening occurs in this region, leading to plastic flow of the material during the cutting process. Although lubricant is sprayed onto the workpiece surface during machining to reduce friction and facilitate heat dissipation, this phenomenon cannot be entirely avoided. In the smooth upper layer of the scale-like structure, material is sheared away and chips continuously accumulate. When chip accumulation reaches a critical level, chip fracture occurs at the root. Moreover, due to the relatively large tool-edge radius of the carbide cutting tool, the fracture process is dominated by a pushing effect rather than pure cutting, resulting in an abrupt fracture layer at the edges of the scale-like patterns. This fracture behavior occurs periodically during machining and ultimately produces the surface morphology observed in the figure. The central region of each micro-pillar is relatively smooth, corresponding to the uncut material surface. In contrast, the edges exhibit noticeable bulging due to plastic deformation. During cutting, a portion of the material that is not fully removed is squeezed toward the uncut region, further increasing the height of the micro-pillar. As a result, the absolute depths measured in **Fig. 7** exceed the preset cutting depth.

The increase in height is primarily attributed to plastic deformation and extrusion effects. The calculated aspect ratios of the microstructures produced under different parameters range from 0.15 to 0.26. Under appropriate processing spacing, reducing the transverse feed distance between adjacent rows or decreasing v_c/f effectively increases the aspect ratio of the micro-pillar structures. When the same cutting tool is used, the aspect ratio increases with cutting depth within a certain range. However, when the cutting depth becomes excessive, the clearance angle of the tool causes interference between the tool flank and the micro-pillar during machining, damaging the formed structures and leading to failure in generating the desired morphology. Under the present processing conditions, the maximum achievable aspect ratio is approximately 0.26, as shown in group PVMT9.

Workpiece	Expected processing photograph	SEM photograph	White light interfero-meter photograph
PVMT1	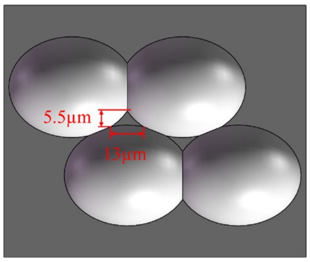	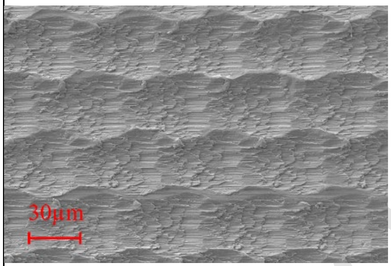	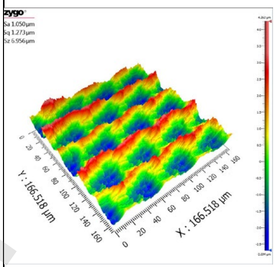
PVMT2	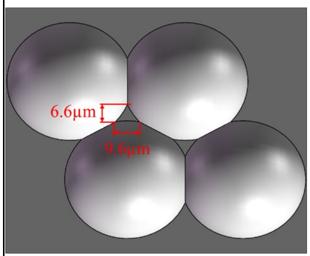	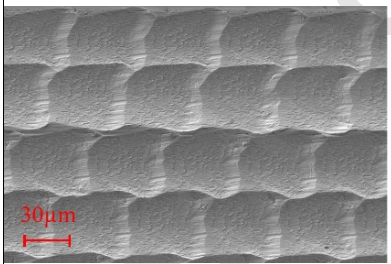	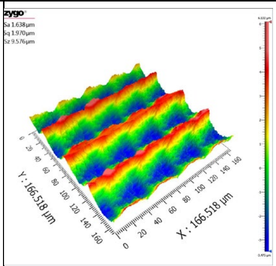
PVMT3	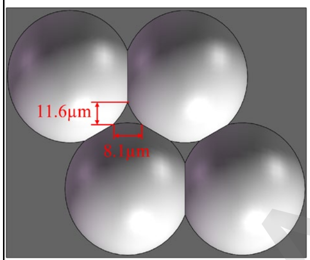	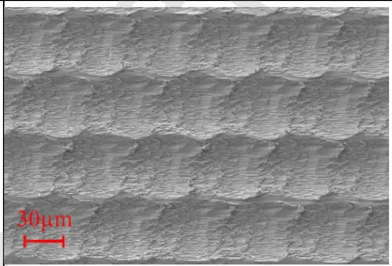	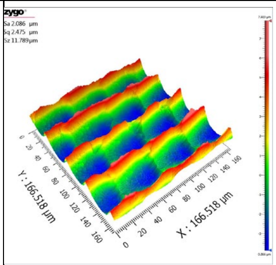
PVMT4	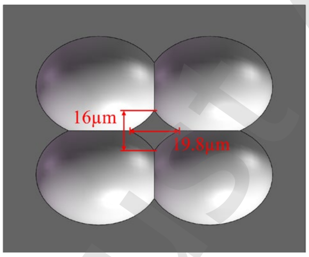	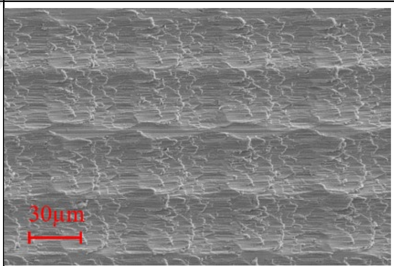	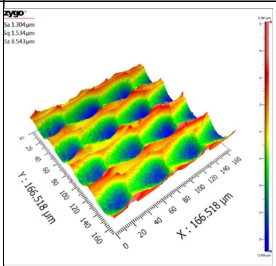
PVMT5	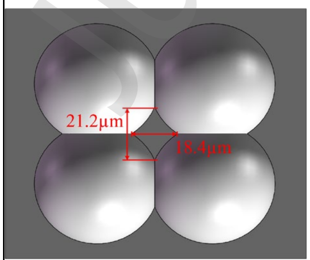	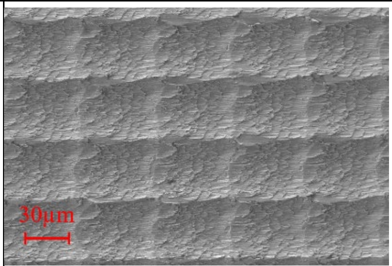	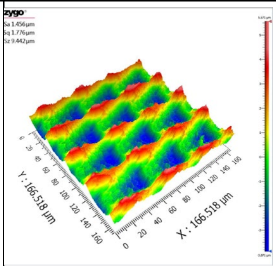
PVMT6	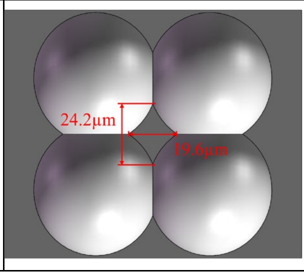	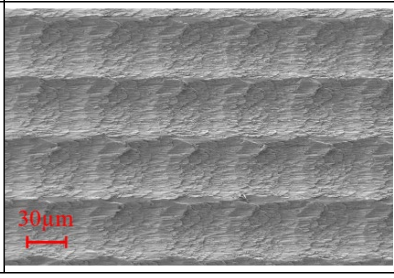	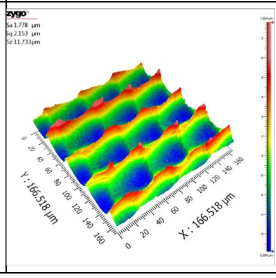

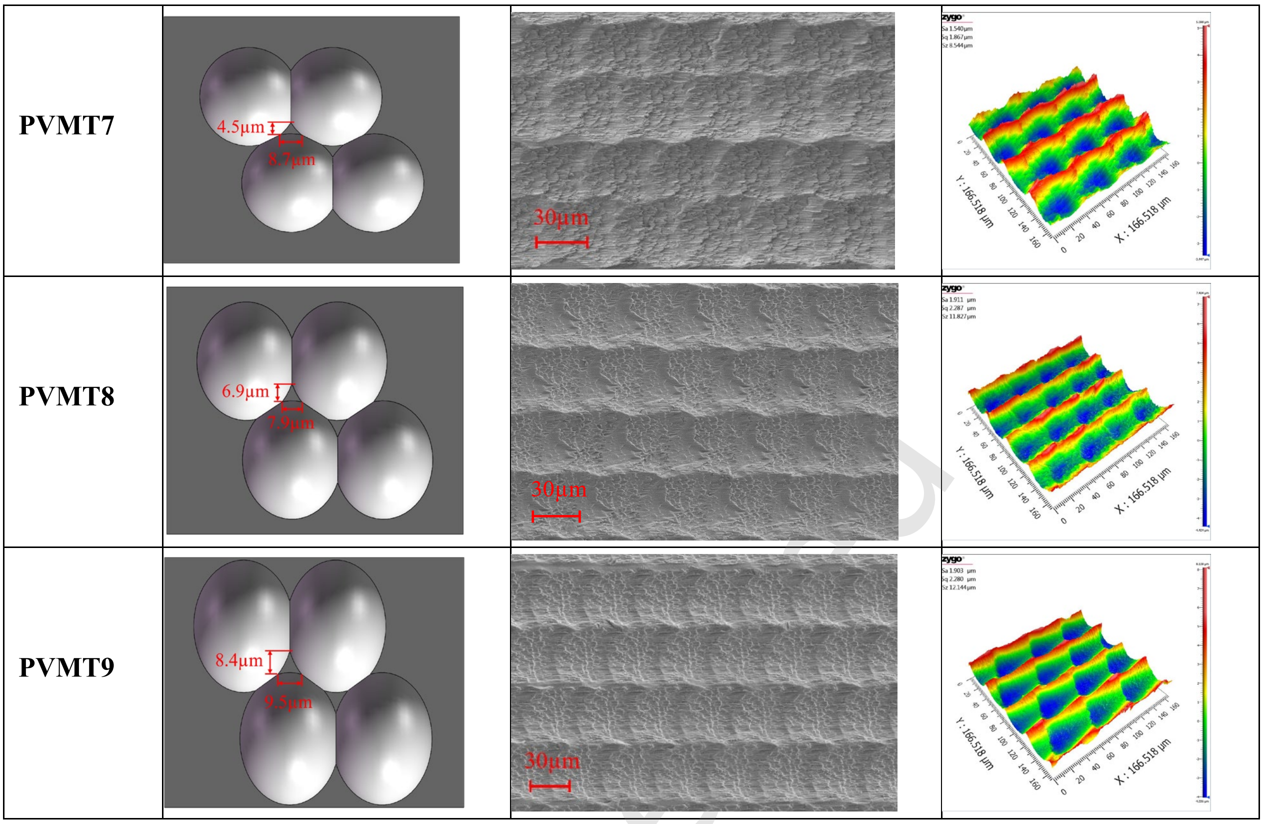

Fig. 7 Characterization of surface morphology of titanium alloy workpieces under different PVMT processing parameters.

4.1.2 Surface wettability determination

After PVMT processing, the hydrophobic performance of the material surface is significantly enhanced, as evidenced by the notable increase in static contact angle, indicating that the microstructure fabrication effectively improves the surface hydrophobicity. **Fig. 8** shows the droplet contact angle measurements of the material surface after PVMT processing. Among them, **Fig. 8**a shows the test results of the PVMT processing groups, while **Fig. 8**a0 displays the results for the untextured sample, whose surface roughness is Sa = 0.09 μm and surface droplet contact angle is 78.6°. **Fig. 8**a1-**Fig. 8**a9 correspond to the nine sets of PVMT parameters shown in **Table 1**. The measured contact angles range from 99.1° to 112.4°, with an average value of 104.5°. Compared with the untextured surface, the average droplet contact angle of the samples processed with this method increases by 25.9°, indicating a significant enhancement in hydrophobicity. Among all processed samples, group PVMT9 exhibits the highest droplet contact angle of 112.4°.

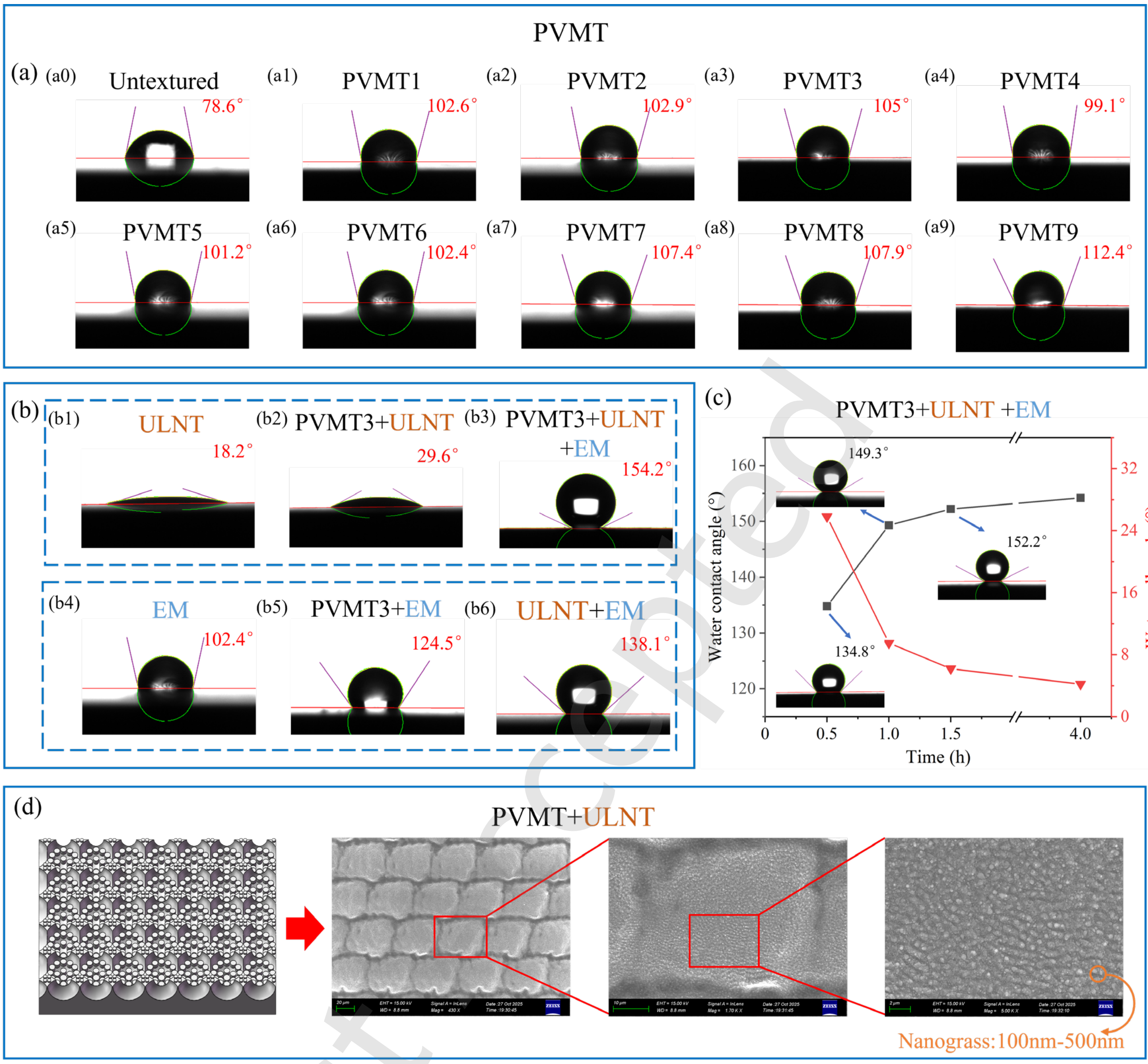

Fig. 8 Surface wettability measurement results. (a) Surface wettability test results with PVMT processing. (b) Surface wettability test of PVMT3 under different machining processes. (c) Group PVMT3&ULNT surface contact angle and roll contact angle test after different time of EM treatment. (d) SEM image of PVMT3 with ULNT processed.

According to the test results, when the cutting speed is kept constant, adjusting the lateral feed distance and elliptical vibration parameters increases the cutting depth and improves the aspect ratio of the micro-pillars, thereby enhancing the surface hydrophobicity. When the aspect ratio increases by 0.07, the droplet contact angle increases by approximately 3.5°. When all other processing parameters remain unchanged and only the phase difference of the microstructure in the longitudinal direction is altered, the staggered arrangement of micro-pillars further improves hydrophobicity compared with longitudinally aligned structures, increasing the droplet contact angle by about 3°. In addition, under constant processing parameters, modifying v_c/f to adjust the lateral length of the micro-pillars and thereby increase their aspect ratio also enhances hydrophobicity. When the aspect ratio increases by 0.04, the droplet contact angle rises by approximately 5.7°.

These findings demonstrate that the micro-pillar structures fabricated via PVMT significantly enhance the surface hydrophobicity. By altering surface roughness, the structure enables droplets to remain suspended on top of the micro-pillars, trapping a large amount of air beneath them and greatly reducing the actual solid–liquid contact area. As a result, the processed surfaces exhibit superior hydrophobic performance compared with unprocessed surfaces.

4.1.3 Underwater drag test of PVMT processing group

Underwater drag test results indicate that the PVMT fabricated microstructures exhibit significant drag reduction effects. **Fig. 9** presents the drag measurements for surfaces processed by PVMT. The experiments were conducted within a Reynolds number range of 2.62E+4 to 1.04E+5. As shown in **Fig. 9**d, PVMT processed samples reduced surface drag by 6.7%–13.5% under different Reynolds numbers. The nine sample groups achieved average drag reduction rates of 8.6%–12.6%, and the overall average drag reduction rate was 10.3%. Among them, PVMT9 achieved the highest average drag reduction at 12.6%. This enhanced drag reduction performance is closely related to the geometric parameters of the micro-pillars. The dimensions of the microstructures influence the boundary layer characteristics, surface wettability, and underwater drag reduction capability. In particular, the synergistic effect of structural depth and width governs the balance between local fluid infiltration resistance and interfacial stability, thereby facilitating air entrapment and increasing the effective slip length. A higher aspect ratio (deeper and narrower structures) favors the formation of a stable Cassie–Baxter state, effectively trapping air within the microstructures to form a gas cushion. Consequently, the solid–liquid contact area is reduced, leading to enhanced surface hydrophobicity and improved drag reduction performance.

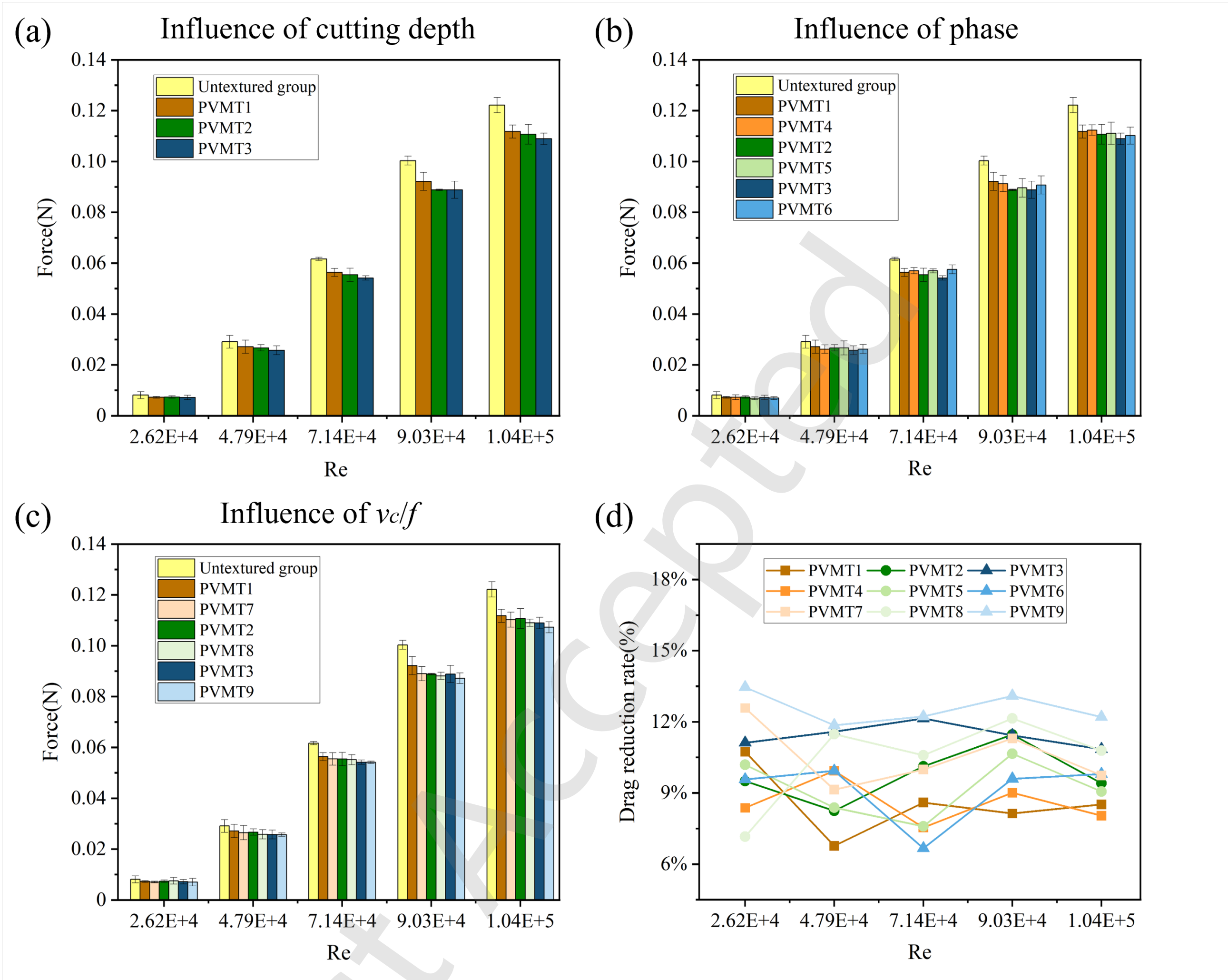

Fig. 9 Underwater drag test of samples processed by PVMT. (a) Influence of cutting depth on underwater drag. (b) Influence of different phases between adjacent processing lines on underwater drag under constant cutting depth. (c) Influence of v_c/f on underwater drag under constant cutting depth. (d) Drag reduction rate of PVMT processing group under different water speeds.

The aspect ratio of the micro-pillars plays a critical role in drag reduction. As shown in **Fig. 9**a, under constant cutting speed, increasing the cutting depth by adjusting the lateral feed distance and the elliptical vibration trajectory parameters raises the aspect ratio of the micro-pillars, thereby enhancing drag reduction performance. When the aspect ratio is increased by 0.07, the underwater resistance can be reduced by about 2%. As shown in **Fig. 9**b, with all other parameters constant, changing only the longitudinal phase arrangement of the microstructures from parallel to staggered (P = 180°) yields a slight additional drag reduction of about 0.2%. As shown in **Fig. 9**c, when the longitudinal phase of the microstructures is fixed and other parameters are unchanged, shortening the lateral length of the micro-pillars and increasing their aspect ratio by adjusting v_c/f can further reduce drag by approximately 1.4%.

4.2 Results after laser scanning processing and energy modification

4.2.1 Morphology change of ULNT machined surface

Femtosecond laser ablation processing of PVMT fabricated samples can generate nanoscale structures on the pre-existing micro-pillars. **Fig. 8**d shows a SEM image of a sample prepared using PVMT3 from **Table 1** after ULNT processing. It can be clearly observed that a layer of uniformly distributed nano-grass structures has grown on the material surface. These structures exhibit a non-periodic morphology with characteristic dimensions ranging from 100 nm to 500 nm. When the femtosecond laser interacts with the titanium alloy surface, the ultrashort high-energy pulses generate extremely high transient temperatures. This elevated temperature leads to localized surface vaporization and accelerates the reaction kinetics between the material and ambient oxygen. In air, oxygen atoms readily react with titanium to form stable oxides, and upon rapid cooling, the generated oxides redeposit onto the surface. Meanwhile, due to the ultrafast laser–matter interaction, multiphoton ionization and strong-field ionization produce a high density of free electrons and localized plasma, resulting in abundant unsaturated surface bonds and lattice defects, which significantly enhance surface chemical reactivity. In addition, reactive oxygen species generated through laser-induced air ionization can react with titanium atoms at relatively low activation barriers, further promoting oxide formation. The oxides formed through these processes are predominantly TiO_2, accompanied by small amounts of lower-valence oxides such as Ti_2O_3 and TiO [44].

These oxides ultimately deposit and reorganize on the surface, forming a dense nano-grass structures. The formation of such nano-grass structures markedly increases the nanoscale surface roughness. The increase in overall surface roughness enhances the adhesion of the subsequent fluorinated layer and lowers the minimum achievable surface energy after EM treatment. Consequently, the superhydrophobic performance and underwater drag reduction capability of the surface are further improved.

4.2.2 Surface wettability determination

The test results of samples subjected to various processing treatments indicate that the PVMT&ULNT&EM composite processing can achieve a stepwise enhancement from hydrophilic to hydrophobic and finally to superhydrophobic performance. **Fig. 8**b presents the droplet contact angle measurements of a micro-pillar sample prepared using PVMT3 from **Table 1**, after undergoing multi-process treatments, to evaluate its hydrophobicity. **Fig. 8**b1 presents the static water contact angle of the sample treated solely by ULNT after being stored in a dust-free environment for 5 days. The measured contact angle was 18.2°, indicating a strongly hydrophilic surface. **Fig. 8**b2 shows the contact angle test results on the material surface after PVMT processing, followed by ULNT post-treatment and 5 days dust-free storage. The laser processing enhanced the surface energy, resulting in temporary hydrophilic properties and the contact angle decreasing to 29.6°. **Fig. 8**b3 shows the contact angle after EM low surface energy modification, where the sample surface demonstrates significantly enhanced hydrophobicity, with the contact angle rising to 154.2°, achieving a typical superhydrophobic state. This demonstrates a strong synergistic effect between the hierarchical micro/nano structures and surface energy treatment: PVMT generated microscale pillars provide the hydrophobic foundation, ULNT generated nanoscale structures further enhance roughness hierarchy, and EM chemical modification finalizes interfacial tuning, collectively enabling stable droplet suspension on the structure tops, significantly reducing solid–liquid contact area and achieving super-hydrophobicity.

Subsequently, the influence of different EM treatment durations on the surface wettability was systematically investigated. As shown in **Fig. 8**c, the PVMT9&ULNT samples were subjected to EM treatment for 0.5 h, 1 h, and 1.5 h, respectively, and measured their static water contact angles and rolling angles.

The results indicate that the static contact angle gradually increased with prolonged EM treatment time. Within the treatment duration range of 1 h to 1.5 h, the contact angle exceeded 150°, demonstrating a pronounced superhydrophobic behavior. Meanwhile, the rolling angle measurements under different treatment times show a decreasing trend as the EM treatment duration increased, indicating reduced droplet adhesion and enhanced self-cleaning performance of the surface.

To further quantify the contributions of different processing methods to hydrophobicity, the study compared contact angle variations for EM, PVMT&EM, ULNT&EM, and PVMT&ULNT&EM. As shown in **Fig. 8**b4, the unprocessed control sample with only EM treatment exhibited a contact angle of 102.4°, indicating that chemical modification alone provides limited hydrophobic enhancement. In contrast, as shown in **Fig. 8**b5, PVMT processing followed by EM treatment increased the contact angle to 124.5°, indicating that micro-pillar structures effectively amplify the EM effect. **Fig. 8**b6 shows that ULNT processing followed by EM yielded a contact angle of 138.1°, higher than the PVMT sample, demonstrating the nanoscale pillars' stronger contribution to droplet suspension. Notably, the PVMT&ULNT&EM composite treatment achieved a contact angle of 154.2°, significantly exceeding all individual cases. These results confirm that the synergy between hierarchical micro/nano structures and surface energy tuning is most effective, minimizing solid–liquid contact area while maintaining low surface energy, thereby achieving superior hydrophobic performance [45].

4.2.3 Element change of material surface of composite processing group

After femtosecond laser ablation, the elemental composition of the material surface changes significantly, notably increasing the surface energy, which causes the material to exhibit hydrophilic behavior. **Fig. 10**a presents the EDS analysis of the untreated sample surface, where the atomic percentage of oxygen is 2.71%. **Fig. 10**b shows the EDS results of the surface after PVMT and ULNT processing, in which the oxygen atomic percentage increases to 8.41%, significantly higher than that of the untreated sample. This substantial increase in oxygen content indicates the formation of titanium oxides on the surface, predominantly TiO_2, which consequently enhances the hydrophilicity of the material surface. Consequently, subsequent fluorination is required to reduce surface energy and significantly improve surface hydrophobicity [46].

(a)

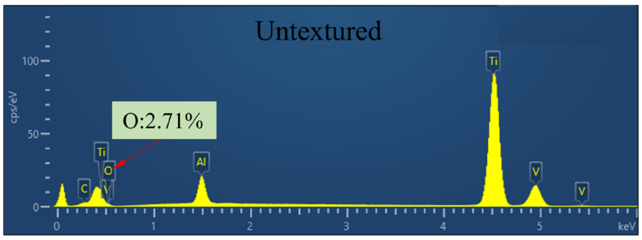

(b)

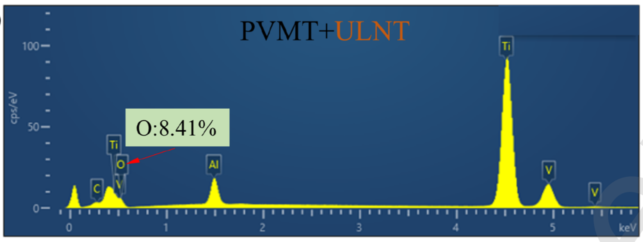

(c)

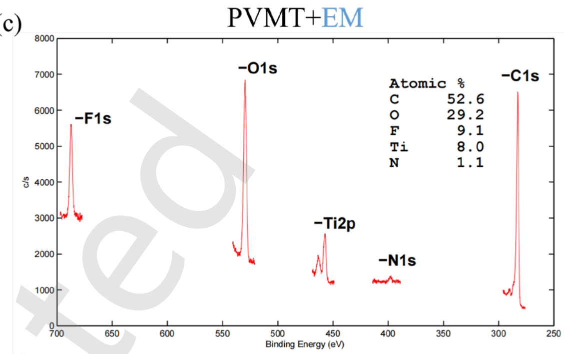

(d)

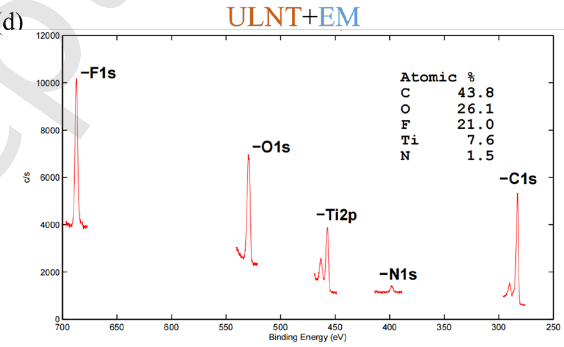

(e)

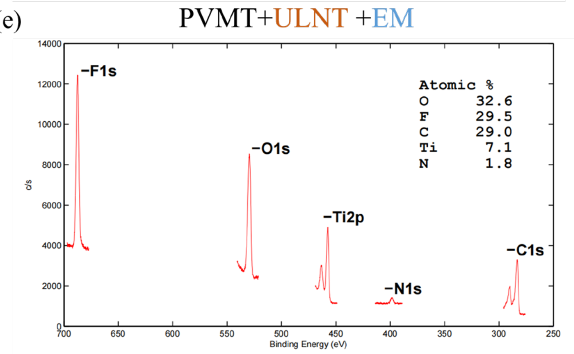

(f)

Elemental Mapping Atomic Percentage(%)		
Fig / Element	Untextured	PVMT+ULNT
C	1.05	1.52
O	2.71	8.41
Al	7.63	6.07
Ti	84.34	80.50
V	4.28	3.50

(g)

Elemental Mapping Atomic Percentage(%)			
Fig / Element	PVMT+EM	ULNT+EM	PVMT+ULNT+EM
C	52.6	43.8	29.0
O	29.2	26.1	32.6
F	9.1	21.0	29.5
Ti	8.0	7.6	7.1
N	1.1	1.5	1.8

(h)

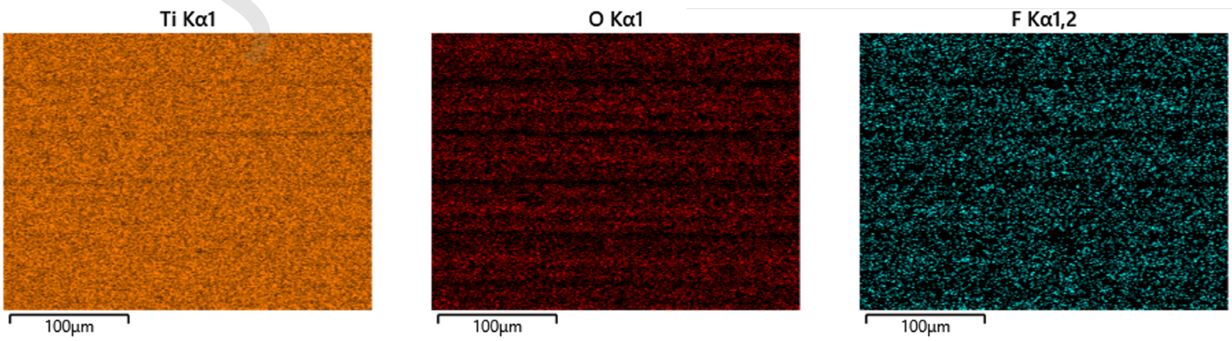

Fig. 10 Element composition of samples surface. (a) Untextured group sample surface EDS element composition. (b) Composition of sample surface EDS elements after PVMT and ULNT processing. (c)

Composition of sample surface XPS elements after PVMT and EM processing. (d) Composition of sample surface XPS elements after ULNT and EM processing. (e) Composition of sample surface XPS elements after PVMT&ULNT&EM processing. (f) Samples surface EDS element composition percentage chart. (g) Samples surface XPS element composition percentage chart. (h) Elemental distribution maps of the surface after PVMT&ULNT&EM processing.

Fig. 10c presents the XPS spectra of the surface elements for the sample prepared using PVMT3 group after EM treatment, showing a surface fluorine atomic percentage of 9.1%. **Fig. 10**d shows the XPS spectra of the sample after ULNT processing followed by EM treatment, where the fluorine atomic percentage increases to 21%. **Fig. 10**e illustrates the XPS results of the sample fabricated using PVMT3 group and subsequently subjected to ULNT and EM treatments, in which the fluorine atomic percentage further increases to 29.5%. **Fig. 10**h displays the elemental distribution maps of Ti, O, and F on the sample surface. As observed, the elements are uniformly distributed over most regions, indicating a relatively continuous and homogeneous coverage of the fluorinated layer. However, in certain localized peak regions, the F signal appears comparatively weaker, suggesting a slightly reduced coverage of the fluorinated layer in those areas.

These results indicate that samples subjected to PVMT and ULNT composite processing exhibit significantly higher fluorine enrichment after EM treatment compared to single process samples. The enrichment of fluorine facilitates the formation of a stable low-energy layer on the material surface, enhancing the material's surface energy regulation under identical conditions, and enabling the sample surface to achieve superhydrophobic properties.

4.2.4 Underwater drag test of composite processing group

Underwater drag tests were conducted on samples processed with the PVMT&ULNT&EM composite method. The results indicate that the composite processed microstructures exhibit superior drag reduction performance. The experiments were conducted within a Reynolds number range of 2.62E+4 to 1.04E+5. **Fig. 11** shows the surface drag measurements at water flow velocities ranging under different Reynolds numbers. As shown in **Fig. 11**d, the surface drag force of the composite treated samples decreased by 12.6%–25.5%. The average drag reduction rate for the nine sample sets ranged from 15.4% to 22.1%, with an overall mean of 18%. Sample 9 demonstrated the best performance, achieving an average drag reduction of 22.1% across the tested velocities, representing one of the highest values reported in the literature. These results highlight the superior potential and significant engineering value of this composite surface processing method for underwater drag reduction.

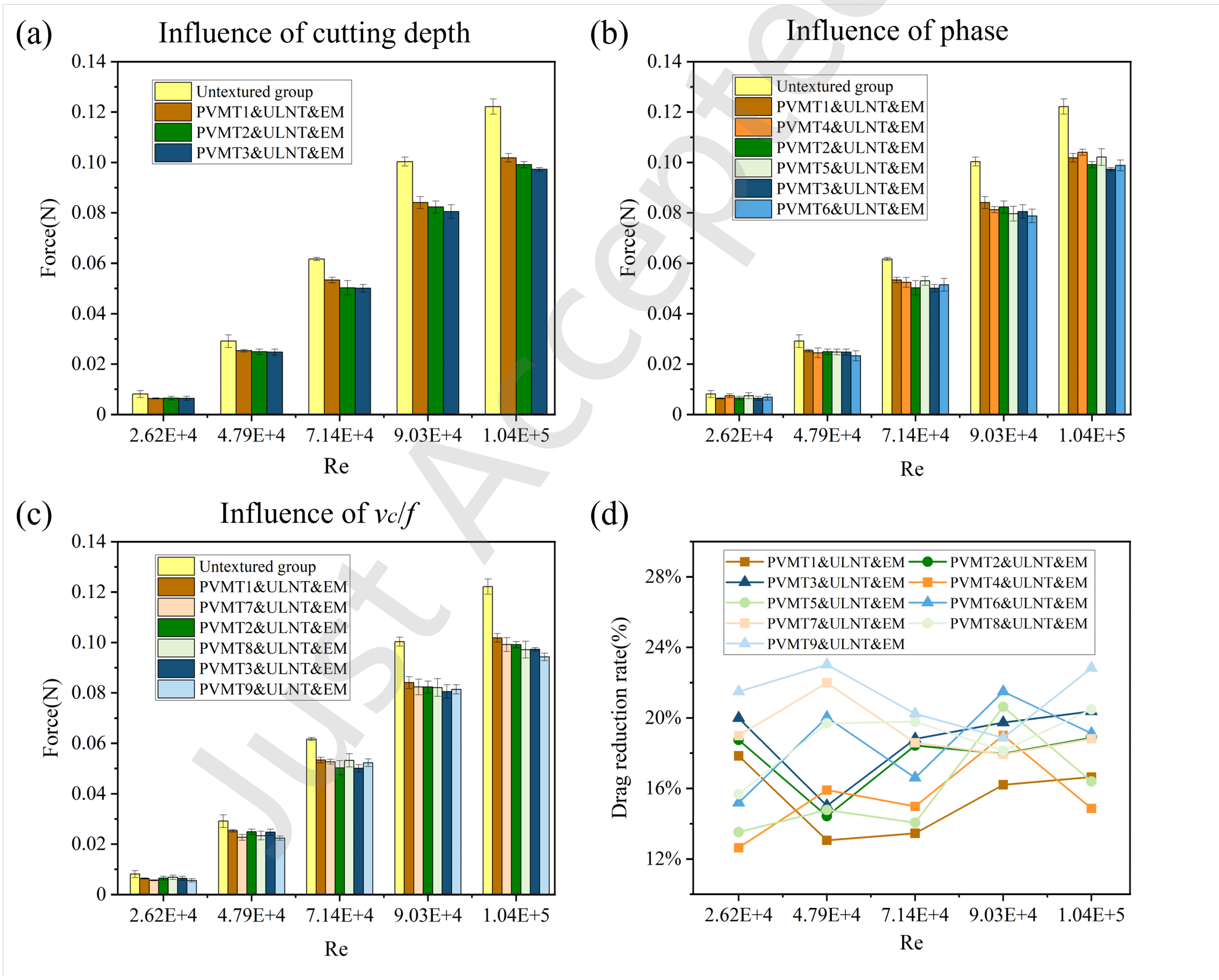

Fig. 11 Underwater drag test of samples processed by PVMT&ULNT&EM. (a) Influence of cutting depth on underwater drag. (b) Influence of different phases between adjacent processing lines on underwater drag under constant cutting depth. (c) Influence of v_c/f on underwater drag under constant cutting depth. (d) Drag reduction rate of PVMT& ULNT&EM processing group under different water speeds.

Drag reduction performance is influenced by micro-pillar size, structure aspect ratio, and longitudinal phase arrangement. As shown in **Fig. 11**a, when other parameters remain constant, increasing the aspect ratio of micro-pillars by adjusting the lateral feed and the elliptical vibration trajectory enhances drag reduction. An increase of 0.07 in the aspect ratio results in an additional 3.1% reduction in underwater surface drag. **Fig. 11**b shows that, with other parameters unchanged, changing the longitudinal phase difference of microstructures from parallel to staggered arrangement further reduces drag by 0.7%. **Fig. 11**c shows that, with a fixed longitudinal phase difference of 180° and other parameters constant, reducing the micro-pillar lateral length via adjusting Vc/f to increase the aspect ratio achieves an additional 2.7% drag reduction.

In summary, samples processed with PVMT, followed by ULNT and EM treatment, exhibit excellent underwater drag reduction performance, with an average reduction rate of 18% and a maximum reduction reaching 22.1%.

4.3 Durability and recovery of underwater resistance performance

4.3.1 Durability test of underwater resistance performance

To systematically evaluate the durability of the underwater drag reduction performance of the fabricated surface, three sets of continuous durability experiments were conducted using the PVMT9&ULNT&EM samples. First, to simulate long-term hydrodynamic scouring conditions, the samples were subjected to continuous dynamic flushing for 8 h at a Reynolds number of 1.04E+5. After the flushing test, the underwater drag reduction performance was re-evaluated over a range of Reynolds numbers. As shown in **Fig. 12**a, the average drag reduction rate after flushing was 17.78%, indicating that the structured surface maintained relatively stable drag reduction performance under high-shear flow conditions.

Second, to assess the influence of complex water chemistry environments on structural stability, the samples were immersed in tap water and seawater collected from the Yellow Sea of China for two months. After immersion, the drag reduction performance was measured again using the same resistance testing apparatus under different Reynolds numbers. As shown in **Fig. 12**b and **Fig. 12**c, the results show that within the effective flow velocity range, the average drag reduction rate was 16.21% after two months of tap water immersion and 12.5% after two months of seawater immersion. These findings demonstrate that although prolonged exposure to aqueous environments leads to a certain degree of degradation of the hydrophobic layer, the hierarchical composite structure still retains considerable drag reduction capability.

4.3.2 Recovery of underwater resistance performance

Since the fluorinated layer may undergo partial hydrolysis or desorption in complex aqueous environments, leading to the degradation of the low-surface-energy layer, a renew fluorination treatment was performed on the three sets of samples after the completion of the durability tests. Specifically, the samples were placed in a constant-temperature drying oven and subjected to re-fluorination under identical processing conditions for 1 h to restore the low-surface-energy surface layer. Subsequently, underwater drag tests were conducted again to evaluate the drag reduction performance under different Reynolds numbers. As shown in **Fig. 12**a, **Fig. 12**b and **Fig. 12**c, the results indicate that, after supplementary fluorination, the drag reduction capability was significantly restored: the sample subjected to 8 h of continuous flushing recovered a drag reduction rate of 22.54%; the sample immersed in tap water recovered to 20.27%; and the sample immersed in seawater recovered to 18.68%.These results demonstrate that the hierarchical micro–nano composite structure developed in this study can effectively regain its low-surface-energy state and drag reduction performance through re-fluorination after degradation of the fluorinated layer, thereby confirming the renewability and potential engineering applicability of the proposed drag reduction system.

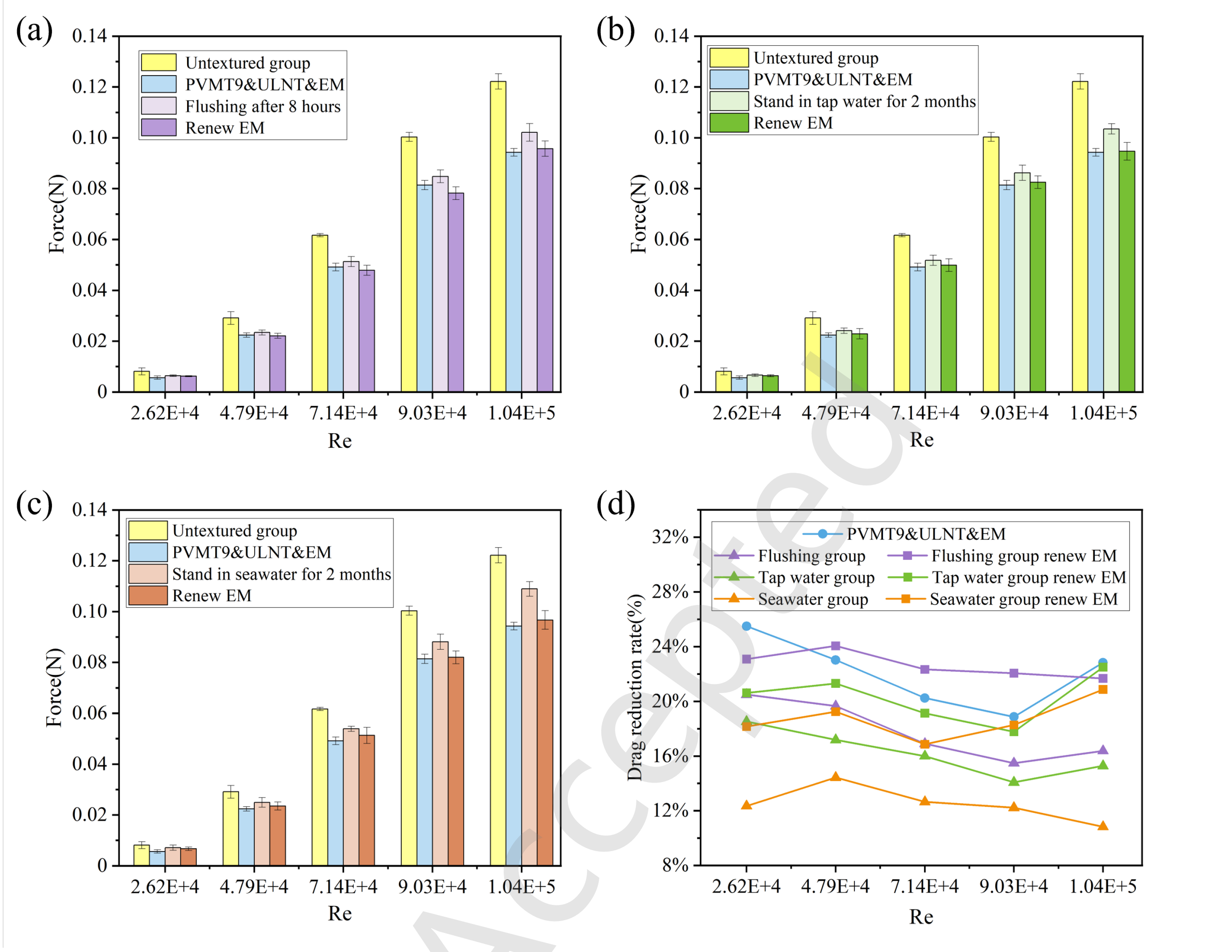

Fig. 12 Durability test and recoverability of underwater resistance capability of workpieces processed by PVMT9&ULNT&EM. (a) Underwater resistance test of the workpiece after 8 hours continuous flushing and subsequent renew EM treatment. (b) Underwater resistance test of the workpiece after two months of tap water immersion and subsequent renew EM treatment. (c) Underwater resistance test of the workpiece after two months of seawater immersion and subsequent renew EM treatment. (d) Drag reduction rate of PVMT9& ULNT&EM processing group under different circumstances.

5 Conclusions

This study addresses the manufacturing requirements for drag reducing functional structures on titanium alloy surfaces by proposing an integrated approach combining PVMT, ULNT, and EM processes to construct hierarchical micro/nano-structured surfaces with superhydrophobic characteristics. Among these, PVMT is a novel technique for the rapid and efficient fabrication of micron-scale pillars on metal surfaces, allowing precise control over the location and dimensions of the microstructures. The feasibility of this process was validated through machining experiments. Systematic evaluation of the samples' surface wettability and underwater drag before and after treatment confirmed the effectiveness of the method. The following conclusions can be drawn from the study:

(1) The method introduces the two-dimensional elliptical vibration into the tool motion, so that the tool enters and exits the material surface periodically in each vibration period, forming controllable micro-pit units. On this basis, precise retention of residual material is achieved by coordinating the phase difference between successive passes with lateral feed, resulting in a periodic and dimensionally controlled array of micro-pillars. Compared with conventional micro-pit fabrication, this method significantly improves the aspect ratio of the surface structures, reaching a maximum of 0.26.

(2) The key parameters of microstructure forming were determined. PVMT enables precise and controllable shaping of micro-pillars through the synergistic adjustment of multiple process parameters. Specifically, varying v_c and f modulates the lateral morphology of the micro-pillars; adjusting f_z controls the longitudinal morphology; changes in the elliptical vibration trajectory and *DOC* modify the aspect ratio; altering P adjusts the overall arrangement of the microstructures. By coupling these parameters, the desired microstructures can be reproducibly fabricated.

(3) PVMT demonstrates outstanding capability in regulating surface wettability. When combined with ULNT and EM, overall hydrophobicity is further enhanced. Compared to smooth workpieces, Ti-6Al-4V surfaces processed with PVMT exhibit significantly improved wettability, with an average increase in contact angle of 25.9°, reaching a maximum of 33.8°. After subsequent ULNT processing and EM treatment, the contact angle reaches 154.2°, achieving a superhydrophobic state. Compared with samples treated only with ULNT and EM, the composite processed samples exhibit superior hydrophobic performance, mainly due to the optimized microstructure morphology and enhanced adhesion of fluorosilane on the surface. After PVMT processing followed by EM treatment, the

fluorine content on the processed surface reaches 0.2%. When ULNT processing is combined with EM treatment, the fluorine percentage increases to 1.1%. With the full PVMT&ULNT&EM composite treatment, the fluorine content is further elevated to 1.85%, indicating a significantly enhanced fluorine enrichment on the surface.

(4) PVMT demonstrates a notable advantage in reducing underwater drag. When combined with ULNT and EM, the drag reduction effect is further enhanced. Compared with smooth workpiece, Ti-6Al-4V surfaces processed with PVMT exhibit excellent drag reduction performance across different Reynolds numbers, with an average reduction of 10.3% and a maximum of 12.6%. After ULNT processing and EM treatment, the average drag reduction further increases to 18%, with a maximum of 22.1%. After undergoing various durability tests, although the drag reduction rate of the surface decreased to some extent, the surface still retained measurable drag reduction capability. Moreover, upon reapplying the fluorinated layer, the drag reduction performance was effectively restored. These results indicate that the hierarchical micro/nano composite structures fabricated via PVMT and ULNT, coupled with EM surface functionalization, offer a significant advantage for underwater drag reduction applications on metal surface.

Author contribution

Bin Zhao: investigation, experiments, writing of original draft, writing including review and editing, and visualization, review and editing, language polishing. Jianfu Zhang: funding acquisition, supervision. Peiyuan Ding: experiments, methodology. Pingfa Feng: review and editing, project administration and supervision. Qilin Li: investigation, methodology. Hang Yu: experiments. Ding Weng: methodology. Daochun Xu: review and editing, project administration and supervision. Jianjian Wang: Conceptualization, review and editing, project administration and supervision.

Funding

The authors gratefully acknowledge the financial support for this research provided by National Natural Science Foundation of China (Grant No. 52475470, 52105458, 124115301), State Key Laboratory of Tribology in Advanced Equipment (Grant No. SKLT2024Z12), State Key Laboratory of High-performance Precision Manufacturing (Grant No. HPMKF202503).

Declarations

The authors declare that they have no known competing financial interests or personal relationships that could have appeared to influence the work reported in this paper.

References

[1] Tang Z Q, Tian T, Molino P J, et al. Recent advances in superhydrophobic materials development for maritime applications[J]. Advanced Science, 2024, 11(16): 2308152.

[2] Shi F, Niu J, Liu J, et al. Towards understanding why a superhydrophobic coating is needed by water striders[J]. Advanced Materials, 2007, 19(17): 2257-2261.

[3] Zhang J, Gabillet C, Billard J Y. Experimental study of the bubbly drag reduction in the recovery region of a separated turbulent boundary layer[J]. International Journal of Multiphase Flow, 2021, 142: 103697.

[4] Wang Z, Tao T, Zhu Y, et al. Water entry dynamics of rough microstructured spheres[J]. Physics of Fluids, 2022, 34(8).

[5] Xu J, Du Z, Huang X, et al. Design and Development of 10,000-Meter Class Autonomous Underwater Vehicle[J]. Journal of Marine Science and Engineering, 2024, 12(11): 2097.

[6] Zhai X, Zhang H, Wang S, et al. Experimental study on the drag reduction of underwater vehicles by drag-reducing agents injection[J]. Applied Ocean Research, 2024, 153: 104303.

[7] Mäkiharju S A, Ceccio S L. On multi-point gas injection to form an air layer for frictional drag reduction[J]. Ocean Engineering, 2018, 147: 206-214.

[8] Zhang L, Wan X, Zhou X, et al. Pyramid-shaped superhydrophobic surfaces for underwater drag reduction[J]. ACS Applied Materials & Interfaces, 2024, 16(33): 44319-44327.

[9] Li Z, Guo Z. Bioinspired surfaces with wettability for antifouling application[J]. Nanoscale, 2019, 11(47): 22636-22663.

[10] Dolid A, Gomes L C, Mergulhão F J, et al. Combining chemistry and topography to fight biofilm formation: Fabrication of micropatterned surfaces with a peptide-based coating[J]. Colloids and Surfaces B: Biointerfaces, 2020, 196: 111365.

[11] Jiang H, Li J, Cao C, et al. Butterfly-wing hierarchical metallic glassy nanostructure for surface enhanced Raman scattering[J]. Nano Research, 2019, 12(11): 2808-2814.

[12] Chen Y, Hu Y, Zhang L W. Effective underwater drag reduction: A butterfly wing scale-inspired superhydrophobic surface[J]. ACS Applied Materials & Interfaces, 2024, 16(20): 26954-26964.

[13] Liu G, Yuan Z, Qiu Z, et al. A brief review of bio-inspired surface technology and application toward underwater drag reduction[J]. Ocean Engineering, 2020, 199: 106962.

[14] Saadatbakhsh M, Asl S J, Kiani M J, et al. Slip length measurement of pdms/hydrophobic silica superhydrophobic coating for drag reduction application[J]. Surface and Coatings Technology, 2020, 404: 126428.

[15] Li D, Guo Z. Metal-organic framework superhydrophobic coating on Kevlar fabric with efficient drag reduction and wear resistance[J]. Applied Surface Science, 2018, 443: 548-557.

[16] Cui X, Liu X, Chen H, et al. Functionalized super-hydrophobic nanocomposite surface integrating with anti-icing and drag reduction properties[J]. Chemical Engineering Journal, 2024, 499: 156093.

[17] Zhang Q, Wang Y, Qin Z, et al. Study on surface fabrication and drag reduction performances of gradient hydrophobic aluminum alloy[J]. Optics & Laser Technology, 2023, 163: 109379.

[18] Guo X J, Xue C H, Sathasivam S, et al. Fabrication of robust superhydrophobic surfaces via aerosol-assisted CVD and thermo-triggered healing of superhydrophobicity by recovery of roughness structures[J]. Journal of Materials Chemistry A, 2019, 7(29): 17604-17612.

[19] Shen L, Fan M, Qiu M, et al. Superhydrophobic nickel coating fabricated by scanning electrodeposition[J]. Applied Surface Science, 2019, 483: 706-712.

[20] Zheng Z, Zhang J, Feng P, et al. Fabrication of hierarchical micro/nanostructures on titanium alloy by combining rotary ultrasonic milling and anodizing[J]. Manufacturing Letters, 2022, 34: 43-48.

[21] Zheng Z, Zhang J, Li Z, et al. Development of a transverse-feeding vibration chiseling process for ultrafast and flexible texturing of metallic micropillars[J]. Journal of Manufacturing Processes, 2025, 133: 734-753.

[22] Ding P, Feng P, Wu K, et al. Review of vibration texturing[J]. Journal of Materials Processing Technology, 2025: 118851.

[23] Wang Z, Liu X, Guo Y, et al. Armored superhydrophobic surfaces with excellent drag reduction in complex environmental conditions[J]. Langmuir, 2024, 40(7): 3766-3773.

[24] Wang J, Liu Y, Yan Y, et al. The mechanisms of material removal and atomic-scale damage in InP during elliptical vibration-assisted nanoscratching integrated with laser processing[J]. Journal of Materials Processing Technology, 2025: 119069.

[25] Sajjady S A, Abadi H N H, Amini S, et al. Analytical and experimental study of topography of surface texture in ultrasonic vibration assisted turning[J]. Materials & Design, 2016, 93: 311-323.

[26] Liu X, Zhang J, Hu X, et al. Influence of tool material and geometry on micro-textured surface in radial ultrasonic vibration-assisted turning[J]. International Journal of Mechanical Sciences, 2019, 152: 545-557.

[27] Wang J, Liao W H, Guo P. Modulated ultrasonic elliptical vibration cutting for ductile-regime texturing of brittle materials with 2-D combined resonant and non-resonant vibrations[J]. International Journal of Mechanical Sciences, 2020, 170: 105347.

[28] Wu H, Huang H, Zhang Z, et al. Micro-amplitude vibration-assisted scratching: a new method for one step and controllable fabrication of the microscale V-groove and nanoscale ripples[J]. International Journal of Extreme Manufacturing, 2025, 7(3): 035102.

[29] Zheng S, Liang X, Li J, et al. Drag reduction using bionic groove surface for underwater vehicles[J]. Frontiers in Bioengineering and Biotechnology, 2023, 11: 1223691.

[30] Li Z, Zhang J, Zheng Z, et al. Elliptical vibration chiseling: a novel process for texturing ultra-high-aspect-ratio microstructures on the metallic surface[J]. International Journal of Extreme Manufacturing, 2024, 6(2): 025102.

[31] Xue B, Yan H, Liu Z, et al. Achieving tip-based down-milling forming of nanograting structures with variable heights through precise control of nano revolving trajectories[J]. International Journal of Extreme Manufacturing, 2025, 7(5): 055101.

[32] Wang J, Wang Y, Zhang J, et al. Blazed grating enables highly decoupled optically variable devices fabricated by vibration-assisted diamond texturing[J]. Optics Express, 2022, 30(6): 8829-8846.

[33] Wu K, Zhang J, Zheng Z, et al. Fabrication of micro/nanostructured copper fibers by vibration cutting for felt-based freshwater purification[J]. Nanomanufacturing and Metrology, 2024, 7(1): 21.

[34] Li Q, Ding P, Li Z, et al. Enhancing tribological performance of metal matrix composites via high-quality micro-dimples patterned by elliptical vibration texturing[J]. Friction, 2025.

[35] Chen C, Feng P, Feng F, et al. Micro/nano-surface modification of titanium implant enhancing wear resistance and biocompatibility[J]. International Journal of Mechanical Sciences, 2024, 276: 109385.

[36] Lu Y, Guo P, Pei P, et al. Experimental studies of wettability control on cylindrical surfaces by elliptical vibration texturing[J]. The International Journal of Advanced Manufacturing Technology, 2015, 76(9): 1807-1817.

[37] Guo P, Ehmann K F. An analysis of the surface generation mechanics of the elliptical vibration texturing process[J]. International Journal of Machine Tools and Manufacture, 2013, 64: 85-95.

[38] Law K Y, Zhao H. Surface wetting: characterization, contact angle, and fundamentals[M]. Basel, Switzerland: Springer International Publishing, 2016.

[39] Wang J, Xu Y, Yan Y, et al. Investigation on nanosecond laser processing of superhydrophobic microstructures on SiCp/Al[J]. Applied Surface Science, 2025: 164695.

[40] Schlichting H, Kestin J. Boundary layer theory[M]. New York: McGraw-Hill, 1961.

[41] Schlichting H, Gersten K. Boundary-layer theory[M]. springer, 2016.

[42] White F M. Fluid mechanics[J]. 1999.

[43] Johnson K L. Contact mechanics[M]. Cambridge university press, 1987.

[44] Florian C, Wonneberger R, Undisz A, et al. Chemical effects during the formation of various types of femtosecond laser-generated surface structures on titanium alloy[J]. Applied Physics A, 2020, 126(4): 266.

[45] Liu G, Yuan Z, Qiu Z, et al. A brief review of bio-inspired surface technology and application toward underwater drag reduction[J]. Ocean Engineering, 2020, 199: 106962.

[46] Haryono M B, Lin K W Y, Waritanant T. Fast fabrication of superhydrophobic Ti-6Al-4V surface using Q-switched nanosecond pulsed laser at 1064 nm and cyclohexane[J]. Heliyon, 2024, 10(18).

Bin Zhao He is currently a master degree candidate in mechanical engineering at Beijing Forestry University, Beijing, China. His research interests mainly include ultrasonic micro-nano manufacturing and application.

Wang Jianjian He is currently an associate professor and doctor supervisor at the Department of Mechanical Engineering, Tsinghua University. He received his Ph.D. degree from Tsinghua University in 2017. His research mainly focuses on vibration-enhanced/enabled advanced machining technology, especially micro/ nano surface texturing technology.